difficulties remain for harvesting and expanding a large number of Schwann cells. Accordingly, it is desirable to establish cells with Schwann cell characteristics from sources other than the PNS that are easy to access, capable of rapid expansion, amenable to survival, and able to integrate into the host tissue to elicit axonal regeneration and to contribute to re-myelination.

Therefore, we previously used bone marrow stromal cells (MSCs) as a source for inducing Schwann cells because MSCs are easily accessible through aspiration of the bone marrow from patients or a marrow bank and can be expanded in culture with fewer ethical problems compared to other sources. MSCs can be readily expanded in large scale for auto-transplantation, and have the potential to differentiate into other kinds of cells such as osteoblasts, adipocytes, and chondrocytes (Pittenger et al., 1999; Prockop, 1997).

Induction of Schwann cells from MSCs is efficiently achieved by first reverting human and rodent MSCs to an undifferentiated state using beta-mercaptoethanol (BME) followed by retinoic acid (RA) treatment and then inducing differentiation by treating them with forskolin (FSK), basic fibroblast growth factor (bFGF), platelet-derived growth factor (PDGF), and neuregulin, all of which are factors related to Schwann cell differentiation (Dezawa et al., 2001). The induced cells are different from the original untreated MSCs, but are morphologically quite similar to Schwann cells and express Schwann cell markers at a high ratio (Dezawa et al., 2001). The effectiveness of this induction system was also demonstrated by other groups in other mesenchymal stem cells such as adipose-derived stem cells (Jiang et al., 2008; Kingham et al., 2007; Xu et al., 2008).

It is noteworthy that human and rodent MSC-derived Schwann cells express myelin-related markers and contribute to re-myelination when transplanted into rat sciatic nerve injury (Mimura et al., 2004; Shimizu et al., 2007), and also effectively promote axonal regeneration and functional recovery in spinal cord injury (Kamada et al., 2005; Someya et al., 2008). These findings demonstrate that MSC-derived Schwann cells are effective for both PNS and CNS regeneration.

To extend this system to clinical application, the safety and effectiveness in higher mammals must be evaluated. The potential for auto-cell transplantation is one of the strong advantages of MSCs. In this study, we estimated the safety and effectiveness of MSC-derived Schwann cells for auto-cell transplantation in a PNS injury model in cynomolgus monkey. The expression of Schwann cell markers in the MSC-derived Schwann cells was confirmed by both immunocytochemistry and reverse transcription-polymerase chain reaction (RT-PCR). Artificial grafts were made by transferring MSC-derived Schwann cells into trans-permeable tubes filled with 3-dimensional collagen, transplanted into the gap between transected median nerve segments, and followed-up for 1 year. No abnormalities were observed in general conditions. In ^{18}F-fluorodeoxygluocose (FDG)-positron emission tomography (PET) scanning, which allows for highly sensitive detection of neoplastic cells, no abnormal accumulation of radioactivity was observed except in regions known to have physiologic accumulations. Cell proliferation assessed by Ki67 immunostaining demonstrated no mass formation and low proliferation of cells. Restoration of the transplanted nerve was confirmed by the hand movement analysis, electrophysiology, and histology.

These results suggest that auto-cell transplantation therapy using MSC-derived Schwann cells is effective and is very likely to be safe for nerve injury. The practical advantages of MSCs is expected to make this system applicable for treatment of spinal cord injury and other neurotrauma or neurodegenerative diseases where Schwann cell transplantation is expected to be effective.

Materials and methods

Animal experiments using cynomolgus monkeys were approved by the Animal Care and Experimentation Committee of the Kyoto University Graduate School of Medicine, Tohoku University Graduate School of Medicine and the National Cardiovascular Center Research Institute. Six adult male cynomolgus monkeys (3 to 4 years of age) were used in this experiment. Cynomolgus monkeys have been broadly used to evaluate the efficiency of transplantation methods particularly in PNS injury models (Ahmed et al., 1999; Archibald et al., 1995; Auba et al., 2006; Hess et al., 2007; Lee et al., 2008). Furthermore, we have previously confirmed the transdifferentiation capacity of MSCs in cynomolgus monkeys, i.e., to be induced into neuronal cells (Nagane et al., 2009). For these reasons, we chose cynomolgus monkeys as the experimental animal in this study.

Isolation of monkey MSCs and Schwann cell induction

Primary monkey MSCs were isolated from the pelvic bone. Bone marrow aspirate (5 ml) was diluted 1:10 using culture medium comprised of alpha-minimum essential medium (MEM), 15% fetal bovine serum (FBS), 2 mM L-glutamine, and kanamycin and incubated at 37 °C, 5% CO_2. After 4 days, non-adherent cells were removed by replacing the medium. Adherent MSCs were expanded when they reached 95% confluence, and were subcultured 4 times, and then finally subjected to the Schwann cell induction.

MSCs were subcultured at a density of 1.76×10^3 cells/cm^2 and incubated in alpha-MEM containing 1 mM BME without serum for 24 h. The culture medium was then replaced with alpha-MEM containing 10% FBS and 35 ng/ml all-trans-RA (Sigma, St. Louis, MO). Three days later, cells were transferred to alpha-MEM containing 10% FBS, 5 μM FSK (Calbiochem, La Jolla, CA), 10 ng/ml bFGF (Peprotech, London, UK), 5 ng/ml PDFG-AA (Peprotech, London, UK), and 200 ng/ml heregulin-ß1-EGF-domain (R&D Systems, Minneapolis, MN) and cultured for 4 to 5 days. These Schwann cells induced from MSCs were called 'M-Schwann cells' in the following sections.

Evaluation of M-Schwann cells

M-Schwann cells were evaluated using both phase-contrast microscopic observation and immunocytochemistry. For immunocytochemistry, the YST-1 cell line was used for positive control (RIKEN, Ibaraki, Japan), monkey naïve MSCs as a negative control, and monkey M-Schwann cells were fixed with 4% paraformaldehyde in 0.02 M phosphate buffered saline (PBS). Primary antibodies used for the immunocytochemistry were anti-protein zero (P0) rabbit IgG (1:300, kindly provided by Dr. J.J. Archelos, Karl-Franzens Universitat, Graz, Austria), anti-p75 (nerve growth factor receptor) mouse IgG (1:500, Abcam Cambridge, UK), anti-glial fibrillary acidic protein (GFAP) rabbit IgG (1:300, DAKO, Carpinteria, CA), anti-O4 mouse IgM (1:20, Boehringer Ingelheim GmbH, Ingelheim, Germany), anti-CD90 mouse IgG (1:400, BD Bioscience, Bedford, MA), and anti-smooth muscle actin (SMA) mouse IgG (1:400, LabVision, Newmarket, Suffolk, UK). These primary antibodies were detected by Alexa 568-conjugated anti-rabbit IgG, anti-mouse IgG, or anti-mouse IgM antibodies (Molecular Probes, Invitrogen, Carlsbad, CA). Immunocytochemistry was performed as previously described (Kitada et al., 2001). Briefly, samples were incubated in 20% BlockAce (skim milk, Yukijirushi, Tokyo, Japan) in 0.005% saponin and 50 mM glycine in PBS (SaGlyPBS) for 10 min, incubated with the primary antibody in 5% BlockAce in SaGlyPBS overnight at 4 °C followed by the secondary antibody incubation in 5% BlockAce in SaGlyPBS. Nuclei were counterstained with 4′, 6-diamidino-2-phenylindole (DAPI, Molecular Probes). As for immunostaining against CD90, cells were incubated with anti-CD90 antibody in culture medium at 37 °C, 5% CO_2, washed, fixed with 4% paraformaldehyde in 0.02 M PBS, and further processed for secondary antibody incubation. All images were taken by a confocal laser scanning microscope (CS-1, Nikon, Kawasaki, Japan) with the same laser intensity and detection sensitivity.

Expression of Schwann cell markers in RT-PCR

Total RNA from naïve MSCs and M-Schwann cells was extracted using an RNeasy Mini Kit (Qiagen GmbH, Hilden, Germany) and purified in accordance with the manufacturer's instructions. From 1 μg of total RNA, first-strand cDNA was generated using SuperScript II reverse transcriptase (Invitrogen, Carlsbad, CA). The PCR reactions were performed using Ex Taq DNA polymerase (TaKaRa, Tokyo, Japan). The amplification conditions were: 1 min at 94 °C, 1 min at 60 °C, and 1 min at 72 °C, for 30 cycles (25 cycles for β-actin) and a final incubation at 72 °C for an additional 7 min.

We used the following *Macaca fascicularis* PCR Primers that are specific genes for Schwann cells, and β-actin as internal control. ß-actin sense: 5′-TCTAGGCGGACTGTGACTTAGTTGCGTTAC-3′ and antisense: 5′-AATCAAAGTCCTCGGCCACATTGTAGAACT-3′, GFAP sense: 5′-TGCCCTAGGCTCCATCAGTATT-3′ and antisense: 5′-TCCCAGATACC-CTGAGAGAACCT-3′, Krox20 sense: 5′-AGTACCCCAACAGACCTAG-CAAGA-3′ and antisense: 5′-GCAAACTTTCGGCCACAGTAG-3′, MBP sense: 5′-CCCACACACCCCAATTAGCT-3′ and antisense: 5′-GCATCAC-GCTGACTACTCCTCAT-3′.

M-Schwann cell autologous PNS graft

The composition and construction of the biodegradable conduit and collagen sponge were previously reported (Hisasue et al., 2005). Briefly, the copolymer was composed of 75% L-lactic acid and 25% E-caprolactone. A rotating polytetrafluoroethylene tube 2 mm in diameter was dipped in the copolymer solution, immersed in liquid nitrogen for a few minutes, and air dried at 25 °C for 24 h. The tube used for transplantation was 4 mm long with 2-mm internal and 3-mm external diameters. A solid sample of atelocollagen (Nippon Meat Packers, Osaka, Japan; 70 wt.% type I and 30 wt.% type III collagen) was used for sponge preparation. Atelocollagen was dissolved in HCl aqueous solution to a final concentration of 1.0 wt.%. The collagen solution was whipped on a homogenizer, frozen at −80 °C, and freeze-dried. Collagen sponge was prepared by cutting it into pieces to fill the biodegradable conduit. The fabricated guide tubes and collagen sponge were sterilized with ethylene oxide gas before use. This artificial conduit can hold cells or tissue, which will be a scaffold for supporting axonal regeneration. Also, this artificial conduit is gas permeable so that cells inside the graft are able to survive after transplantation (Mligiliche et al., 2003).

To determine the cell concentration of the artificial grafts, we inspected normal monkey median nerve sections by Giemsa staining. We calculated 250 myelinated axons were contained within an area of 110 μm^2, suggesting 250 Schwann cells are myelinating axons in this square measure. The total transverse area of the monkey median nerve, except for the epineurium, was approximately 1570 μm^2. Based on the average length of a Ranvier's node (~1000 μm), a 1-cm nerve segment is estimated to contain approximately 2×10^6 Schwann cells. Thus, the tube was filled with induced M-Schwann cells at a concentration of 2×10^6 cells suspended in 30-μl 0.01 M PBS per 1-cm tube and incubated in 10% FBS containing alpha-MEM for several hours in 5% CO$_2$ at 37 °C before transplantation. The graft was longitudinally cut and counterstained with Hoechst 33342 to observe the distribution of the cells inside the graft.

Transplantation of autologous M-Schwann cell grafts to median nerve

We chose the median nerve to make the PNS injury model, because this nerve is relatively easily accessible and the function of this nerve is easier to evaluate during the regenerative period, rather than any other nerves in cynomolgus monkey (Archibald et al., 1995). Just before transplantation, the motor nerve conduction study (described below) was performed under ketamine- and xylazine-induced general anesthesia. A 20-mm segment of unilateral median nerve was completely removed 2 cm proximal to the wrist joint of the forearm and the artificial graft was anastomosed to the proximal and distal nerve tips and their neurilemma using 10-0 nylon sutures at both ends. Five monkeys (M-Schwann cell-transplanted group) received auto-cell transplantation of the M-Schwann cells, while two monkeys (the sham-operated group) received transplantation of empty artificial grafts that were not filled with M-Schwann cells. Just after transplantation, a motor nerve conduction study performed again to confirm the absence of CMAP indicated that the median nerve was completely transected. For auto-cell transplantation, M-Schwann cells were all derived from each recipient animal so that no immunosuppression was given after transplantation.

General health and behavior analyses

Weight check and blood tests (urea nitrogen, creatinine, creatine phosphokinase, aspartate amino transferase, alanine transferase, lactate dehydrogenase, platelet, hemoglobin, red blood cells, white blood cells, hematocrit, mean corpuscular volume, mean corpuscular hemoglobin, mean corpuscular hemoglobin concentration, D-dimer and fibrinogen A) were performed every month before and after transplantation.

For behavioral analysis, movements of the hand and thumb, and grip strength for obtaining food of both the transplanted and intact sides were recorded on a video tape and analyzed for evaluation. The criteria for hand motion and functional recovery scores were as follows:

Score 5: Strength of the thumb, hand movement, and frequency of hand use for feeding and general behavior, such as grabbing the cage, are nearly equal between operated and intact sides.

Score 4: Strength of the thumb is asymmetrical, but the frequency of the use of the hands is nearly the same in both sides. Monkey is able to grab, but is unable to pinch small objects less than 1 cm.

Score 3: Monkey can grab the cage, but muscular force of the operated hand is weak. The thumb is contractured. Wrist movement compensates for the weakness of the hand and thumb. The muscle force of the thumb is less than half that of the intact side.

Score 2: Functional recovery is weak. Movement of the thumb is observed, but compensation by the wrist is recognized. The use of the operated hand during feeding is rare.

Score 1: Little hand and finger motion on the operated side. Monkey is unable to grab objects.

Score A: Unmeasurable. Monkey is unable to make contact because of too much guarding.

The evaluation was conducted by a person, who did not operate animals, without any information about the animal including the procedure of transplantation, and the observation period after the transplantation.

Motor nerve conduction study

To estimate the restoration of nerve function, we performed motor nerve conduction study at five time points for each animal, just before and after transplantation and at 3, 6, and 12 months after the transplantation. To record the compound muscle action potential (CMAP) in the motor nerve conduction study, we pasted the anode electrode plate on the skin of the palmar side at the proximal joint of the first digit, the cathode electrode plate on the belly muscle of the abductor pollicis brevis, and the ground plate on the back of the forearm (Someya et al., 2008). The median nerve was stimulated with a rectangular wave-shaped pulse using a bipolar stimulator by placing its cathode at either of the following sites; 5-cm proximal to the wrist joint (3 cm proximal to the transplanted site) and at the cubital fossa. At each stimulation site, we applied electrical current of supramaximal intensity (varying from 5 mA to 25 mA) within a range that did not induce ulnar nerve stimulation. For each study, we recorded the CMAP, distal latency (time latency between the stimulus

at the wrist and the increase in the CMAP), and the distance (the length between the recording electrode and the stimulator at the wrist). We used the amplitude of the CMAP and distal velocity (distal latency divided by the distance) for further analysis. For the motor nerve conduction study, we used an EMG/evoked potential measuring system (Neuropack μ, MEB-9100, Nihon Koden, Tokyo, Japan). We used SPSS (ver. 12.0, SPSS Inc., Chicago, IL) for the statistical analysis.

PET using ^{18}F-FDG

For the ^{18}F-FDG-PET scan, we injected ~185 MBq of ^{18}F-FDG produced at the National Cardiovascular Center Research Institute using a conventional method described previously (Hamacher et al., 1986) and scanned the whole body for 48 min starting at 60 min after the injection. For the PET scan, we used a PET scanner (PCT-2000A, Toshiba Medical Systems Corp, Tokyo, Japan) that provided 47 slices in an axial field of view of 162 mm with an intrinsic resolution of 6.2 mm (trans-axial) and 6.0 mm (axial) in full-width-at-half-maximum. The scan was performed in a three-dimensional mode after the transmission scan using three rotating ^{68}Ga–^{68}Ge rod sources. The images were reconstructed in a matrix of $128 \times 128 \times 223$ (x, y, z) with a voxel size of $5.15 \times 5.15 \times 5.15$ mm (x, y, z) using a filtered back projection algorithm. The reconstructed ^{18}F-FDG radioactivity image (in Bq/ml) was scaled by the injected dose of ^{18}F-FDG per body weight of animal (Bq/g) to calculate images of SUV. The region was considered to be abnormal when the SUV value was greater than 2.5 (Al-Sugair and Coleman, 1998), and when located in the area outside of organs known to have physiologic accumulation of FDG (brain, heart, urinary tracts, and kidneys). SUV images were inspected by coronal, axial, and sagittal sections and also by the maximum intensity projection.

Immunohistochemical analysis of transplanted grafts

One year after transplantation, animals were sacrificed by an overdose of pentobarbital and perfused transcardially with 4% paraformaldehyde in 0.01 M PBS. The transplanted median nerve, including the proximal site, graft, and distal site, was dissected out and incubated in the same fixative for 6 h at 4 °C. Tissues were washed with 0.1 M PBS overnight at 4 °C, immersed in 10%, 20%, and 30% sucrose–PBS for 3 h each at 4 °C, embedded in OCT, and cut into 10-μm-thick frozen sections using a cryostat. Immunohistochemistry was performed as described elsewhere (Kitada et al., 2001). Primary antibodies used for immunohistochemistry were: anti-neurofilament (NF) rabbit polyclonal antibody (Sigma), anti-myelin-associated glycoprotein (MAG) mouse monoclonal antibody (1:100, Boehringer Ingelheim, Ingelheim am Rhein, Germany), anti-Ki67 rabbit monoclonal SP-6 IgG (1:300), and anti-CD163 mouse monoclonal IgG (1:20, Hycult Biotechnology, Uden, Netherlands). Secondary antibodies were: anti-rabbit IgG conjugated to Alexa488 (Molecular Probes) and anti-rabbit or anti-mouse IgG conjugated to Alexa568 (Molecular Probes). To assess the extent of regeneration, the ratio of the NF-positive area inside the grafted tube at the middle of the graft was calculated in three 10-μm-thick transverse sections from each animal. Statistical analysis of the ratio of NF-positive area to the total nerve area was compared using ANOVA with pairwise comparison using t-tests. To analyze the distribution of proliferating cells inside the grafted tube, immunostaining against Ki67 was done under the antigen retrieval technique using microwave (Kitada and Rowitch, 2006).

Results

Schwann cell induction from cynomolgus monkey MSCs

Cultured naïve MSCs of cynomolgus monkey are shown in Fig. 1A. When naïve MSCs were treated with BME followed by RA administration, and a set of cytokines (bFGF, FSK, PDGF, and neuregulin), their morphology changed similar to human and rat M-Schwann cells (Figs. 1B–D), suggesting the possibility of Schwann cell induction from monkey MSCs. Cells exhibiting morphological changes were evaluated to determine whether they had acquired Schwann cell phenotypes. In immunocytochemistry, Schwann cell markers including p75, GFAP, P0, and O4 became positive in monkey M-Schwann cells, while naïve MSCs or M-Schwann cells without primary antibody incubation (data not shown) showed no immunoreactivity against
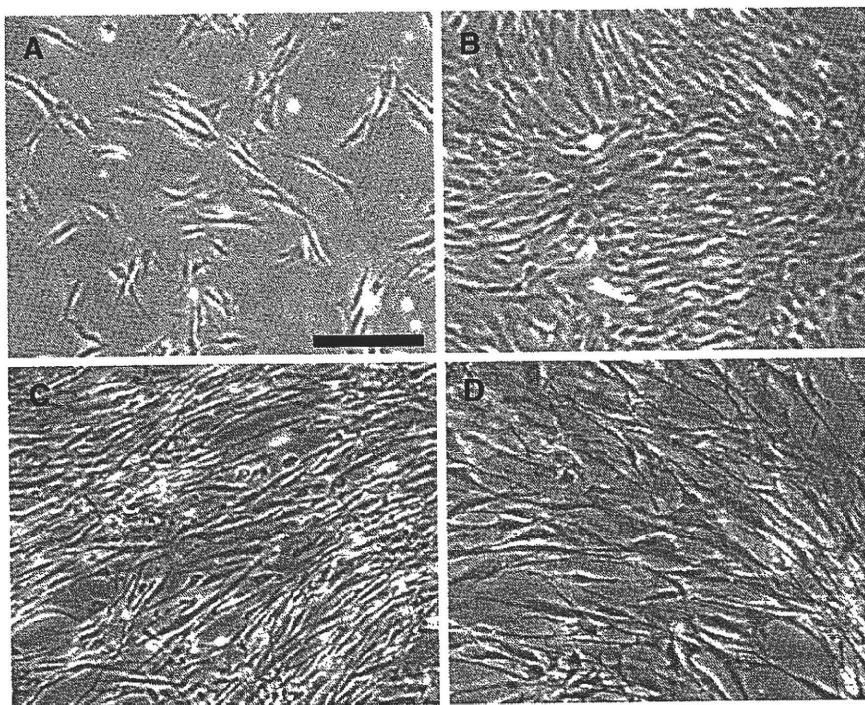

Fig. 1. Phase contrast microscopy. A: Naïve monkey MSCs, B: monkey M-Schwann cells, C: human M-Schwann cells, and D: rat M-Schwann cells. Morphological changes were evident from A to B. M-Schwann cells derived from human and rat exhibited similar morphology to those from monkey. Scale bar: 30 μm.

these Schwann cells markers (Fig. 2). Schwann cell markers analyzed were all positive in the YST-1 cells. The rate of p75-positive cells in M-Schwann cells was estimated to be $99.0 \pm 0.01\%$ (mean $\pm$ SD). RT-PCR showed the mRNA expression of GFAP and Krox20 was weakly detected in naïve MSCs, but was up-regulated following M-Schwann cell induction. Myelin basic protein (MBP), another marker for Schwann cells, was undetectable in naïve MSCs but became clearly detectable in M-Schwann cells (Fig. 3). These results suggested that M-Schwann cells expressed markers and factors related to Schwann cell properties. We tried to determine whether M-Schwann cells sustained their expression of MSC markers such as CD90 and SMA (Supplementary Fig. 1). Whereas CD90 was not expressed in M-Schwann cells, SMA expression was recognized and the expression level of SMA was varied in each M-Schwann cell. These findings suggest that M-Schwann cells might partially trail some of the MSC characteristics at least in culture, although it is unknown whether M-Schwann cells lose or retain the MSC property during maturation in the transplanted environment.

Prior to transplantation, we constructed the graft tube made with lactic acid and E-caprolactone and filled the inside of the graft tube with collagen sponge and M-Schwann cells (see Materials and methods). Cell number was calculated to mimic endogenous Schwann cell number in an intact monkey peripheral nerve. To observe the distribution of the cells inside the graft, the graft was longitudinally cut and the nuclei of the cells were counterstained with Hoechst 33342 (Supplementary Fig. 2). Nuclei of the cells were homogenously distributed inside the graft.
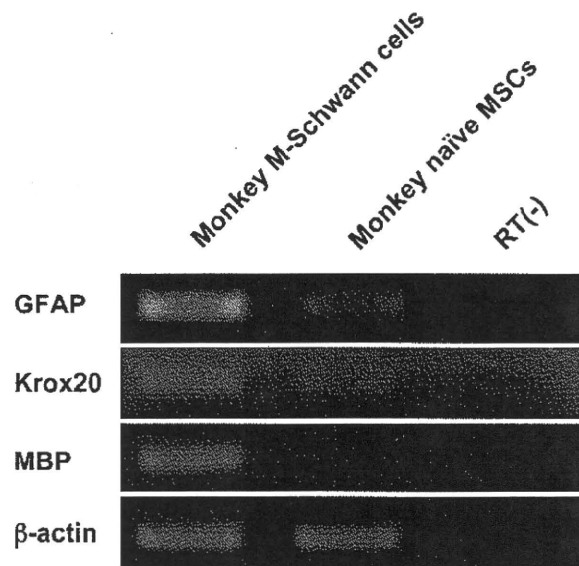

Fig. 3. RT-PCR of Schwann cell markers. Naïve MSCs slightly expressed for mRNA of GFAP and Krox20, but did not express that of myelin basic protein (MBP). Monkey M-Schwann cells, however, presented up-regulation of GFAP and Krox20 mRNA, and became clearly positive for MBP.
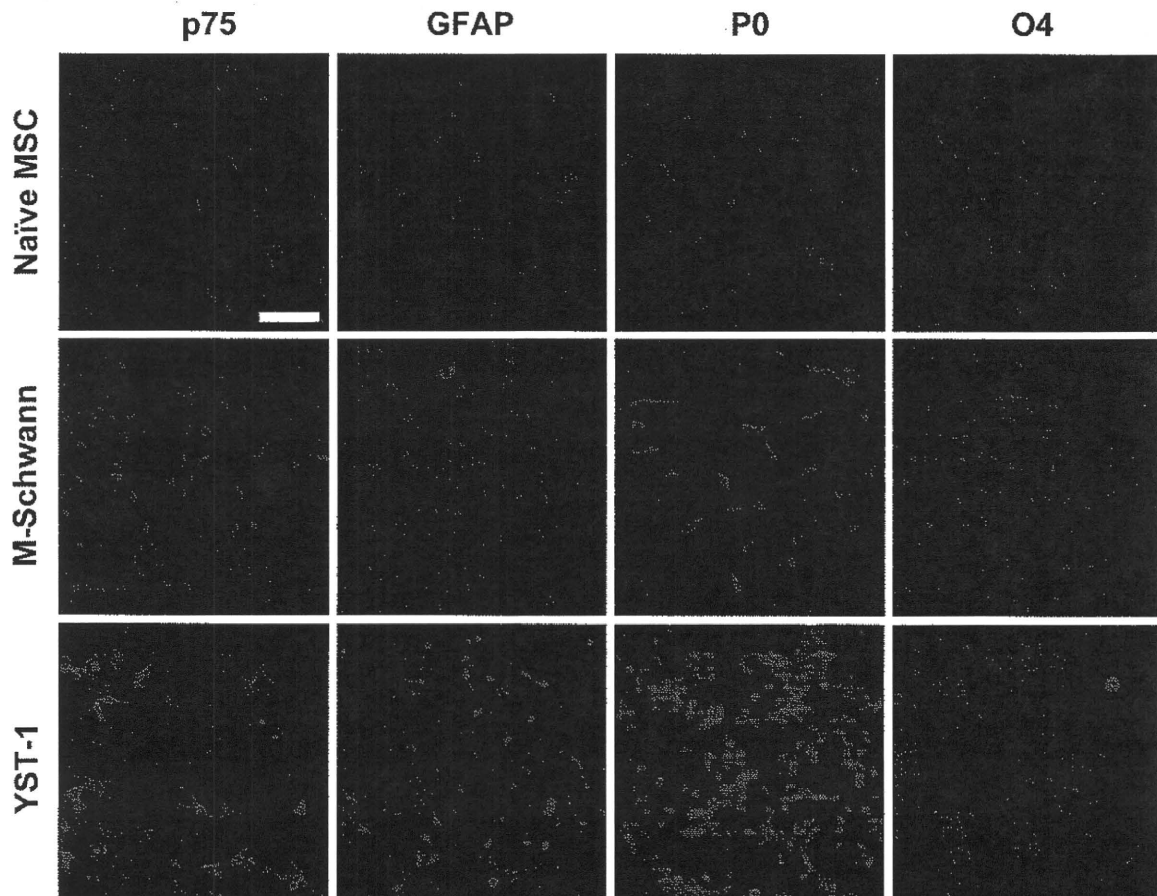

Fig. 2. Immunocytochemistry of naïve MSCs and M-Schwann cells. Initially naïve MSCs exhibited almost no immunoreactivity for Schwann cell markers (red) such as p75, GFAP, P0, and O4. After induction of Schwann cells, M-Schwann cells were positive for all Schwann cell markers: p75, GFAP, P0, and O4. YST-1 was used as a positive control and was also positive for all Schwann cells markers analyzed. DAPI (blue) was used for the counterstaining of nuclei. Scale bar: 50 μm.

Table 1
Body weight (kg).

Group	Animal	Pre	3 m	6 m	12 m
M-Schwann cell-transplanted group	mon0038	4.2	5.1	5.5	5.4
	mon0039	4.8	5.3	5.3	4.9
	mon0044	3.8	4.3	4.5	4.9
	mon0046	3.8	4.3	4.7	4.5
Sham-operated group	mon0045	4.1	4.5	4.8	5.0
	mon0050	3.7	2.8	2.8	3.7

Body weight (kg) is shown at four time points: before transplantation (pre), and at 3, 6, and 12 months after transplantation (3 m, 6 m, and 12 m, respectively).

Table 3
Scores for hand motion recovery.

Group	Animal	3 m	6 m	9 m	12 m
M-Schwann cell-transplanted group	mon0038	3	4	5	5
	mon0039	3	4	5	5
	mon0044	4	4	5	5
	mon0046	4	A	4	4
Sham-operated group	mon0045	1	1	2	2
	mon0050	A	A	1	1

Scores for hand motion recovery at 3, 6, 9, and 12 months after surgery. In the sham-operated group, score 2 was the highest score achieved at 1 year, whereas the M-Schwann cell-transplanted group showed good recovery up to score 5.

General health follow-up

Grafts filled with autologous M-Schwann cells were transplanted to the unilateral median nerve in the M-Schwann cell-transplanted group (monkey numbers: mon0038, mon0039, mon0044, and mon0046). For the sham-operated group, tubes without cells were transplanted (monkey numbers: mon0045 and mon0050). Motor nerve conduction velocity was measured just before and after transplantation to confirm the complete transection of the median nerve.

For follow-up of general health, body weight check and blood tests were performed at 1 to 6 month intervals after transplantation. In both the M-Schwann cell-transplanted and sham-operated groups, no considerable weight loss was observed, except in one animal in the sham-operated group (mon0050; Table 1). Creatinine, creatine kinase, glutamate oxaloacetate transaminase, glutamate pyruvate transaminase, lactate dehydrogenase, platelet, hemoglobin, red blood cell, and white blood cell levels were within normal range in the M-Schwann cell-transplanted group. Blood urea nitrogen was slightly elevated (Table 2). The animals in the sham-operated group also showed elevated blood urea nitrogen and glutamate oxaloacetate transaminase, glutamate pyruvate transaminase, and lactate dehydrogenase higher than normal values. Although the normal values of D-dimer and fibrinogen A are not established in the intact cynomolgus monkeys, the values were almost within the normal range of humans and did not increase during the follow-up period in either group.

Behavioral analysis

To assess functional recovery, general behavior, hand motion, and movement of muscles along the distribution of the affected median nerve were video-recorded and evaluated to be in 5 levels (see Materials and methods). The functional recovery score of the M-Schwann cell-transplanted group was high at 3 months while that of the sham-operated group was markedly lower even at 1 year. In the sham-

operated group, because the use frequency was very low, and hand motion or food grabbing were poor due to the rigidity of the operated hand, their scores remained around 1 and 2. The M-Schwann cell-transplanted group had a mean functional recovery score of approximately 3 and 4 at 6 months. At 9 and 12 months, some monkeys in the M-Schwann cell-transplanted group achieved the highest possible score of 5 (Table 3). Actual hand movements used in feeding are shown in the video-recorded data (see movies in Supplementary information).

Any animals both in the sham-operated and M-Schwann cell-transplanted groups did not exhibit self-mutilation or overgrooming in the radial palm of the hand, the innervation area of sensory branch of the transected median nerve, suggesting no abnormal sensation including dysethesia or hyperalgesia was evoked by transplanted tube and M-Schwann cells.

Motor nerve conduction study

We analyzed the amplitude of the CMAP and the distal velocity, both measured in each animal at five time points (just before and after transplantation, and 3, 6, and 12 months after transplantation; Fig. 4). The group comparison at each observation period was done by the two sample sign test, showing significant differences at 6 and 12 months after transplantation between the M-Schwann cell-transplanted and sham-operated groups. At 12 months after transplantation, the CMAP in M-Schwann cell-transplanted group nerves recovered to ~60% (mean $\pm$ SD $= 7.27 \pm 4.41$ mV) than that of the pre-transplanted nerves (12.2 ± 0.73 mV). The sham-operated CMAP reached ~20% (2.45 ± 0.51 mV). The whole data of each experimental group was further analyzed by the two-way repeated analysis of variance (repeated ANOVA) with factors of group (M-Schwann cell-transplanted vs. sham-operated) and the observation period and found a significant effect of group in CMAP. The M-Schwann cell-transplanted group had a significantly greater CMAP ($F_{1,4} = 5.02$, one-

Table 2
Results of the blood analysis.

	M-Schwann cell-transplanted group ($n=4$)				Sham-operated group ($n=2$)				Normal values ($n=27$)
	Post-1	Post-2	Post-3	Post-4	Post-1	Post-2	Post-3	Post-4	
WBC ($\times 10^2$/µl)	116 (19)	123 (27)	107 (17)	88 (14)	122 (17)	111 (1)	117 (6)	77 (53)	133 (57)
RBC ($\times 10^4$/µl)	554 (50)	567 (59)	565 (51)	576 (56)	562 (10)	580 (5)	497.5 (67)	540 (18)	587 (77)
Hb (g/dL)	13.1 (0.5)	13.5 (0.8)	13.25 (0.5)	13.7 (1.5)	13.0 (0.3)	13.5 (0.4)	12.9 (0.8)*	12.6 (0.1)	14.6 (1.1)
PLT ($\times 10^4$/µl)	35.4 (14.0)	32.5 (10.0)	30.2 (7)	32.5 (11)	38.0 (3.6)	31.0 (0.1)	31.5 (0.5)	30.2 (5.0)	37.9 (10.8)
GOT (IU/L)	29 (5)	28 (3)	29 (4)	36 (6)	32 (2)	46 (9)*	38 (5)	25 (1)	31 (8)
GPT (IU/L)	15 (1)	26 (3)	27 (5)	34 (7)	31 (21)	64 (33)*	64 (7)**	30 (5)	36 (12)
LDH (IU/L)	437 (182)	337 (30)	377 (25)	479 (116)	343 (80)	511 (123)	401 (62)	265 (35)	592 (116)
CRE (mg/dL)	0.7 (0.1)	0.7 (0.1)	0.7 (.01)	0.7 (0.1)	0.6 (0.0)	0.7 (0.0)	0.7 (0.1)	0.7 (0.1)	0.66 (0.12)
BUN (mg/dL)	23.9 (3.5)	28.1 (4.3)**	25.6 (4.2)*	19.8 (6.1)*	27 (1.0)	30.2 (7.8)*	25.1 (2.4)	19.1 (5.7)	20.5 (3.7)
CK (U/L)	147 (66)	128 (32)	69 (23)	214 (93)**	158 (44)	303 (86)**	229 (200)*	553 (4)**	126 (50)
D-dimer (µg/ml)	0.7 (0.1)	1.2 (0.3)	0.9 (0.3)	–	1.3 (0.5)	1.3 (0.2)	1.1 (0.1)	–	–
Fibrinogen A (mg/dl)	–	170 (23)	190 (20)	–	–	176 (1.4)	205 (13)	–	–

Values are presented as mean (SD). For each animal, blood was sampled at four time points: 55–104 days (Post-1), 110–180 days (Post-2), 196–217 days (Post-3), and 350–470 days (Post-4) after transplantation. Normal values were obtained from animals 3 years old or younger. –: not obtained. *one or **two animals in the corresponding group had values outside the normal range of values $\pm$ 2SD. Although normal D-dimer and fibrinogen A values were not obtained in cynomolgus monkeys, they were close to the normal range of humans (D-dimer: <1.0 mg/ml and fibrinogen A <380 mg/dl).
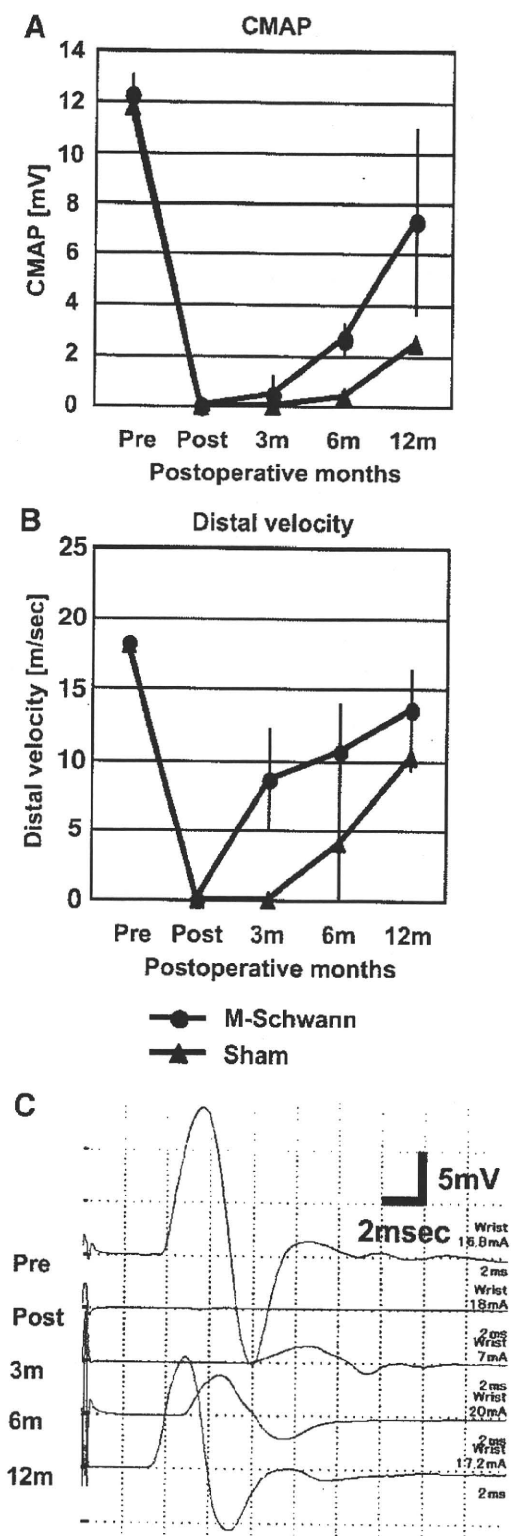
Fig. 4. Results of motor nerve conduction studies. (A) Compound muscle action potential (CMAP, in mV) of the medial nerve, (B) distal velocity (m/s) of the median nerve and (C) the actual wave forms of the CMAP for an example of the M-Schwann cell-transplanted group. Pre; before transplantation, Post; just after transplantation, 3 m, 6 m, and 12 m indicate 3, 6, and 12 months after transplantation, respectively. Values in (A, B) are presented as mean ± SD (mV and m/s, respectively).

the transected site and that this graft contributed about 40% of the grab function at 1 year post-transplantation. In terms of distal velocity, significant promotion was observed at 3 months after transplantation by the two sample sign test, and a significant group effect ($F_{1,4} = 5.85$, one-tailed $P = 0.036$) was demonstrated by the two-way repeated ANOVA, in the M-Schwann cell-transplanted group, but the velocities at 12 months after transplantation were well recovered in both the M-Schwann cell-transplanted group (13.5 ± 4.03 m/s) and the sham-operated group (10.2 ± 1.33 m/s) to a level 60% to 75% of the pre-transplantation (18.0 ± 0.57 m/s) velocity. These findings suggest that saltatory conduction was a little accelerated by the transplanted M-Schwann cells but reached almost a similar level observed in the sham-operated group at 12 months after transplantation because of the contribution of the host Schwann cells in myelin formation and saltatory conduction.

^{18}F-FDG-PET

Although the ^{18}F-FDG-PET test is not completely specific for neoplastic cells, it sensitively detects such cells in most organs. In addition, previous studies revealed that neoplastic transformation of host Schwann cells can be detected by FDG-PET scans (Hamada et al., 2006). Thus, for each animal, we performed ^{18}F-FDG-PET scans to screen for neoplastic transformation of the grafts at 3, 6, and 12 months after transplantation.

We found no abnormal radioactivity accumulation based on standardized uptake value (SUV) images of FDG-PET at any of the three time points (Fig. 5) except in regions of physiologic accumulation and in the vein where the FDG was injected. Importantly, no apparent accumulation was observed at the transplanted site of the animals in any PET scan.

Histological analysis of the graft after 1 year

To estimate the safety of M-Schwann cell transplantation, labeling of cells prior to the transplantation such as lentivirus- or retrovirus-mediated gene introduction of green fluorescent protein or labeling with fluorescent dye was not performed. Therefore, the true ratio of Schwann cell marker expression in transplanted M-Schwann cells could not be evaluated. Furthermore, since host Schwann cells migrate from both proximal and distal nerve segments, host Schwann cells and M-Schwann cells might have intermingled within the grafted tube. For these reasons, we did not attempt to show the grafted cells inside the tube but instead examined the effect of transplanted cells. The effect of Schwann cells in the injured PNS is to promote axonal regeneration and to construct the myelin sheath for saltatory conduction (Fawcett and Keynes, 1990; Hall, 2001; Radtke and Vogt, 2009; Torigoe et al., 1996). Electrophysiological data suggested that transplanted M-Schwann cells contributed to the promotion of axonal regeneration and that myelination level was not significantly different between the M-Schwann cell-transplanted and sham-operated groups. In this regard, we evaluated the effect of transplanted cells by immunohistochemistry for NF to detect the amount of regenerated axons inside the grafted tube (McKay Hart et al., 2002). The immunohistochemistry for NF in the transverse sections of the middle portion of the grafted tube is shown in Fig. 6. Also, the NF-positive axons inside the tube seemed more condensed, particularly at the site just beneath the inner wall of the tube, in the M-Schwann cell-transplanted group compared to the control group (Figs. 6C and D). The ratios of the NF-positive area to the total nerve area in each animal were calculated (see Materials and methods) as 51.5 ± 7.55% and 33.3 ± 1.11% in the M-Schwann cell-transplanted and sham-operated groups, respectively. The ratio of the NF-positive area in the M-Schwann cell-transplanted group was significantly greater than that in the sham-operated group (one-tailed $P < 0.05$, Student's t-test with Bonferroni correction). The NF-positive area

tailed $P = 0.04$) than the sham-operated group. These findings suggest that auto-cell transplantation of M-Schwann cells significantly promoted regeneration of the median nerve motor axons distal to
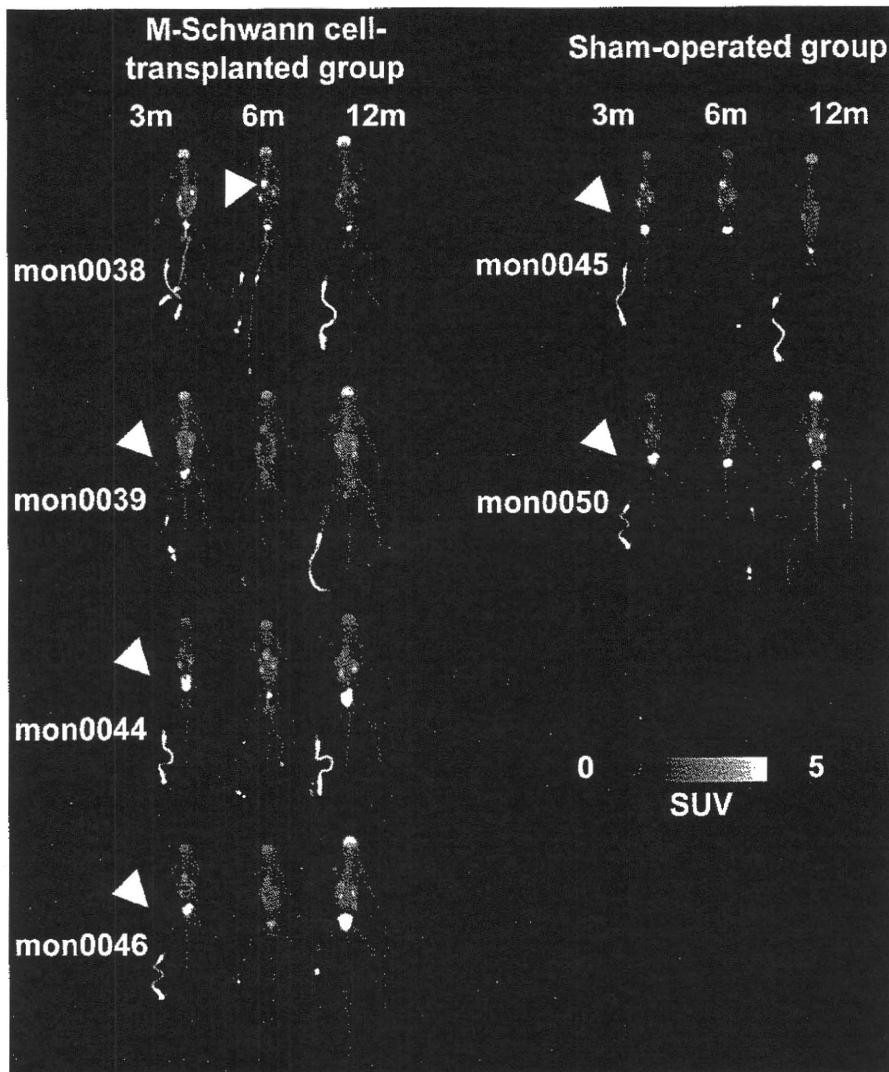
Fig. 5. Results of the whole-body ^{18}F-fluorodeoxyglucose (FDG)-positron emission tomography (PET) performed to screen for neoplastic transformation of the grafted cells. In PET images, the frontal view of the animal is presented by maximal intensity projection. Arrowheads indicate the grafted sites, the distal median nerve (left in mon0038, and right in the other animals). Abnormal accumulation (cut-off = 2.5 in SUV) was not observed in any PET scan except in regions known to have physiologic accumulations of FDG: brain, heart, kidney, urinary tracts, and injection site. SUV: standardized uptake value. 3 m, 6 m, and 12 m indicate 3, 6, and 12 months after graft transplantation.

significantly correlated with the CMAP measurement just before autopsy (measured at 12 months after operation; Pearson's correlation coefficient = 0.81, $P < 0.05$). While transplanted M-Schwann cells were not distinguishable from host Schwann cells, double-immunostaining for NF and MAG on transverse sections both of the M-Schwann cell-transplanted and sham-operated groups (Figs. 6E and F, respectively) confirmed myelination of regenerated axons. As was predicted by results of electrophysiology taken at 12 months, the extent of myelination was almost similar in both experimental groups. These data suggest that the improvement observed in behavioral and electrophysiological assessment was provided by transplanted M-Schwann cells in regard to their function in promoting axonal regeneration rather than in facilitation of myelination of regenerated axons.

To observe the immune response against the transplanted graft, immunohistochemistry against CD163, a specific marker for monocytes and macrophages, was performed (Supplementary Fig. 3). Inside the graft, CD163+ cells were scarcely observed at the middle portion of the graft and some cells were found near (<300 μm) by the wall of the graft. Although CD163+ cells were observed inside the graft, the number of CD163+ cells inside the graft in the M-Schwann cell-

transplanted group was as small as 1.50 ± 0.41 cells in 0.1 mm² and was not significantly different from 1.44 ± 0.51 cells, that in the sham-operated group, indicating that the sustained rejection of transplanted M-Schwann cells was not prominently exerted after transplantation. More CD163+ cells were observed in the wall of the graft both in the sham-operated and M-Schwann cell-transplanted groups, indicating the process of bio-degradation of the grafted tube.

Local tumor formation was evaluated by the detection of proliferating cells with Ki67-immunostaining (Fig. 7), showing no statistically significant difference between Ki67-positive cells inside the grafted tube in the M-Schwann cell-transplanted and sham-operated groups: 2.88 ± 0.67 cells and 3.25 ± 1.00 cells/0.1 mm², respectively. Also, these proliferating cells exhibited no mass formation. These findings indicate that transplanted M-Schwann cells did not exhibit local tumor formation.

Discussion

In the present study, we estimated the safety and effectiveness of transplanting M-Schwann cells into non-human primates over a 1-year period. Schwann cells induce neural regeneration and enable
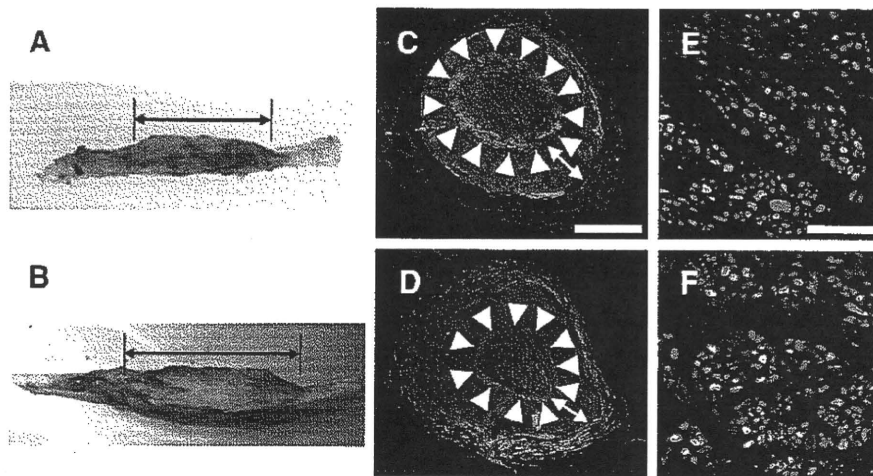
Fig. 6. Grafted monkey median nerves at 12 months. (A, B) Appearance of grafted monkey median nerves. Arrows indicate approximate position of grafts in mon0039 (M-Schwann cell-transplanted group) (A) and mon0045 (sham-operated group) (B). (C–F) Immunohistochemistry of transverse sections in the middle portion of the graft in mon0039 (M-Schwann cell-transplanted group) (C, E) and mon0045 (sham-operated group) (D, F). Immunostaining for neurofilament (NF) (green) exhibited massive axonal regeneration just beneath the inner wall of the tube (arrowheads) in the M-Schwann cell-transplanted group (C), but not in the sham-operated group (D). Arrows in C and D indicate the wall of the grafted tube. Immunofluorescence against NF (green) and myelin-associated glycoprotein (red) showed myelination of regenerated axons (E, F). The extent of myelination of regenerated axons was almost similar in both experimental groups. DAPI (blue) was used for the counterstaining of nuclei. Scale bars: 500 μm (C, D) and 40 μm (E, F).

saltatory conduction by producing myelin, and are expected to be applied to PNS and CNS injuries. In the case of the monkey study, PNS injury models are easily approved by the ethics committee for animal experimentation rather than spinal cord injury. We therefore examined the effectiveness and safety of our system in a monkey median nerve injury model. Cells that expressed Schwann cell markers could be efficiently induced from cynomolgus monkey MSCs, similar to rat and human MSCs (Dezawa et al., 2001, Shimizu et al., 2007). Auto-cell transplantation of M-Schwann cells in monkey median nerve injury model resulted in successful nerve regeneration and functional recovery.

Cell labeling is effective in tracing the fate of transplanted cells and this method is categorized into two techniques such as exogenous gene introduction and staining with a fluorescent dye. Gene introduction by virus infection such as lentivirus or retrovirus enables permanent cell labeling, while this method is also known to evoke a hazardous risk of carcinogenesis (Hacein-Bey-Abina et al., 2003). Fluorescence dyes such as DiI or PKH26 have been used for cell labeling for transplantation study but these dyes also have cytotoxicity and might not exhibit sufficient fluorescence intensity after prolonged period such as 1 year. For these reasons, we did not perform labeling of M-Schwann cells in this study. Based on the lack of any signs of tumor formation in FDG-PET scanning and in immuno-histochemistry for proliferation marker for up to 1 year in any of the M-Schwann cell-transplanted animals, and the absence of serious
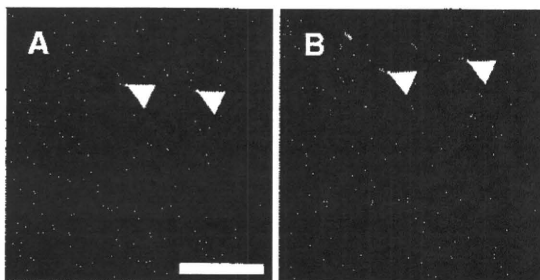

Fig. 7. Immunohistochemistry inside the grafted tube. Small numbers of Ki67-positive cells (red, arrowheads) were found in both the M-Schwann cell-transplanted (A) and also sham-operated (B) groups. DAPI (blue) was used for the counterstaining of nuclei. Scale bar: 100 μm.

problems in the general health and histological study, our system is very likely to be safe. In our previous report, M-Schwann cells induced from human MSCs were transplanted into a rat model of sciatic nerve transection under immunosuppression, and were shown to contribute to re-myelination of regenerating axons and functional recovery (Shimizu et al., 2007). Also, we previously examined the safety of M-Schwann cells induced from human MSCs transplanted into uninjured nude-mice striatum followed-up for 6 months (unpublished data). Tumor formation was not observed in pathologic analysis and the general health of transplanted nude-mice showed no serious problems. These results together support the idea that human MSC-derived Schwann cells may also be safe and effective for cell-based therapy.

Our results indicate that the M-Schwann cells contributed to functional recovery after transplantation in the injured PNS. Electro-physiology demonstrated that CMAP was much improved in the M-Schwann cell-transplanted group compared with the sham-operated group, suggesting regeneration of a larger number of axons promoted by the transplanted M-Schwann cells in this group. This concept was confirmed by histological analysis. The area positive for NF, being considered to be correlated with CMAP, was larger in the M-Schwann cell-transplanted group than in the sham-operated group.

In previous studies, we have demonstrated the myelin formation of M-Schwann cells induced from rat MSCs after transplantation into the injured PNS models even in the ultrastructural level (Dezawa et al., 2001; Ishikawa et al., 2009). In this study, electrophysiological data regarding distal velocity was accelerated in the M-Schwann cell-transplanted group compared with those of the sham-operated group. However, the biodegradable conduit used in this study itself has the property to support regenerating axons (Hisasue et al., 2005). As mentioned in Results, host Schwann cells also join to promote axonal regeneration and to form myelin sheath. This process might be enhanced by the biodegradable conduit used in this study and might mask the function of M-Schwann cells on saltatory conduction at later observation period such as 6 and 12 months after transplantation. Whether the transplanted M-Schwann cells can form myelin sheath to contribute efficient saltatory conduction should be assessed in future studies by labeling cells with either a genetic modification or fluorescent dyes prior to transplantation.

Because the induction system for M-Schwann cells comprises a cell density adjustment at the first step followed by a series of treatments with BME, RA, and a set of cytokines, M-Schwann cells can be induced

by a rather simple and stable process without gene introduction, and thus the system is a realistic source of cell therapy for PNS and CNS regeneration. The induction of cells with Schwann cell properties was recently reported in embryonic stem cells and skin-derived neural crest cells, but their effectiveness and safety in terms of tumor formation and problems that might arise need to be examined because of potential ethical concerns (Roth et al., 2007).

MSCs provide potential possibilities for clinical application, since they can be efficiently expanded in vitro to acquire a therapeutic scale. Different from embryonic stem cells or fetus/embryo-derived cells, MSCs are easily accessible through aspiration of the bone marrow, and can be easily expanded in large scale for auto-transplantation. MSCs can be collected without serious ethical problems, and there is no need to use fertilized eggs or fetuses, which is a great advantage for clinical use. In addition, as MSCs are also obtained from marrow banks, transplantation of induced cells with the same HLA subtype from a healthy donor may minimize the risks of rejection in allo-transplantation.

In the present study, we chose the PNS injury model to show the safety and efficiency of M-Schwann cells, in which M-Schwann cells were induced prior to, and transplanted immediately after, the injury. This model, however, is not a representative of clinical situations. Virtually, it needs more than 1 week to prepare M-Schwann cells after harvesting MSCs. Further studies are necessary for confirming the effectiveness of M-Schwann cells in delayed transplantation in PNS injury.

Our previous studies have demonstrated that Schwann cells induced from MSCs exert trophic effects, provide a strong foothold for regenerating axons, and re-construct myelin to support saltatory conduction (Dezawa et al., 2001; Ishikawa et al., 2009; Kamada et al., 2005; Mimura et al., 2004; Shimizu et al., 2007; Someya et al., 2008). Therefore, induced Schwann cells are a valuable candidate source for cell therapy in peripheral nerve injury, and this study suggests that auto-cell transplantation of M-Schwann cells is also hopeful for application to spinal cord injury.

Acknowledgments

Appendix A. Supplementary data

Supplementary data associated with this article can be found, in the online version, at doi:10.1016/j.expneurol.2010.01.022.

References

Ahmed, Z., Brown, R.A., Ljungberg, C., Wiberg, M., Terenghi, G., 1999. Nerve growth factor enhances peripheral nerve regeneration in non-human primates. Scand. J. Plast. Reconstr. Surg. Hand Surg. 33, 393–401.

Al-Sugair, A., Coleman, R.E., 1998. Applications of PET in lung cancer. Semin. Nucl. Med. 28, 303–319.

Archibald, S.J., Shefner, J., Krarup, C., Madison, R.D., 1995. Monkey median nerve repaired by nerve graft or collagen nerve guide tube. J. Neurosci. 15, 4109–4123.

Auba, C., Hontanilla, B., Arcocha, J., Gorria, O., 2006. Peripheral nerve regeneration through allografts compared with autografts in FK506-treated monkeys. J. Neurosurg. 105, 602–609.

Bunge, M.B., 2002. Bridging the transected or contused adult rat spinal cord with Schwann cell and olfactory ensheathing glia transplants. Prog. Brain Res. 137, 275–282.

Bunge, M.B., 2008. Novel combination strategies to repair the injured mammalian spinal cord. J. Spinal Cord Med. 31, 262–269.

Dezawa, M., Adachi-Usami, E., 2000. Role of Schwann cells in retinal ganglion cell axon regeneration. Prog. Retin. Eye Res. 19, 171–204.

Dezawa, M., Takahashi, I., Esaki, M., Takano, M., Sawada, H., 2001. Sciatic nerve regeneration in rats induced by transplantation of in vitro differentiated bone-marrow stromal cells. Eur. J. NeuroSci. 14, 1771–1776.

Fawcett, J.W., Keynes, R.J., 1990. Peripheral nerve regeneration. Annu. Rev. Neurosci. 13, 43–60.

Hacein-Bey-Abina, S., Von Kalle, C., Schmidt, M., McCormack, M.P., Wulffraat, N., Leboulch, P., Lim, A., Osborne, C.S., Pawliuk, R., Morillon, E., Sorensen, R., Forster, A., Fraser, P., Cohen, J.I., de Saint Basile, G., Alexander, I., Wintergerst, U., Frebourg, T., Aurias, A., Stoppa-Lyonnet, D., Romana, S., Radford-Weiss, I., Gross, F., Valensi, F., Delabesse, E., Macintyre, E., Sigaux, F., Soulier, J., Leiva, L.E., Wissler, M., Prinz, C., Rabbitts, T.H., Le Deist, F., Fischer, A., Cavazzana-Calvo, M., 2003. LMO2-associated clonal T cell proliferation in two patients after gene therapy for SCID-X1. Science 302, 415–419.

Hall, S., 2001. Nerve repair: a neurobiologist's view. J. Hand Surg. [Br] 26, 129–136.

Hamacher, K., Coenen, H.H., Stocklin, G., 1986. Efficient stereospecific synthesis of no-carrier-added 2-[18F]-fluoro-2-deoxy-D-glucose using aminopolyether supported nucleophilic substitution. J. Nucl. Med. 27, 235–238.

Hamada, K., Tomita, Y., Ueda, T., Enomoto, K., Kakunaga, S., Myoui, A., Higuchi, I., Yoshikawa, H., Hatazawa, J., 2006. Evaluation of delayed 18F-FDG PET in differential diagnosis for malignant soft-tissue tumors. Ann. Nucl. Med. 20, 671–675.

Hess, J.R., Brenner, M.J., Fox, I.K., Nichols, C.M., Myckatyn, T.M., Hunter, D.A., Rickman, S.R., Mackinnon, S.E., 2007. Use of cold-preserved allografts seeded with autologous Schwann cells in the treatment of a long-gap peripheral nerve injury. Plast. Reconstr. Surg. 119, 246–259.

Hill, C.E., Moon, L.D., Wood, P.M., Bunge, M.B., 2006. Labeled Schwann cell transplantation: cell loss, host Schwann cell replacement, and strategies to enhance survival. Glia 53, 338–343.

Hisasue, S., Kato, R., Sato, Y., Suetomi, T., Tabata, Y., Tsukamoto, T., 2005. Cavernous nerve reconstruction with a biodegradable conduit graft and collagen sponge in the rat. J. Urol. 173, 286–291.

Ishikawa, N., Suzuki, Y., Dezawa, M., Kataoka, K., Ohta, M., Cho, H., Ide, C., 2009. Peripheral nerve regeneration by transplantation of BMSC-derived Schwann cells as chitosan gel sponge scaffolds. J. Biomed. Mater. Res. A 89, 1118–1124.

Jiang, L., Zhu, J.K., Liu, X.L., Xiang, P., Hu, J., Yu, W.H., 2008. Differentiation of rat adipose tissue-derived stem cells into Schwann-like cells in vitro. NeuroReport 19, 1015–1019.

Kamada, T., Koda, M., Dezawa, M., Yoshinaga, K., Hashimoto, M., Koshizuka, S., Nishio, Y., Moriya, H., Yamazaki, M., 2005. Transplantation of bone marrow stromal cell-derived Schwann cells promotes axonal regeneration and functional recovery after complete transection of adult rat spinal cord. J. Neuropathol. Exp. Neurol. 64, 37–45.

Kingham, P.J., Kalbermatten, D.F., Mahay, D., Armstrong, S.J., Wiberg, M., Terenghi, G., 2007. Adipose-derived stem cells differentiate into a Schwann cell phenotype and promote neurite outgrowth in vitro. Exp. Neurol. 207, 267–274.

Kitada, M., Chakrabortty, S., Matsumoto, N., Taketomi, M., Ide, C., 2001. Differentiation of choroid plexus ependymal cells into astrocytes after grafting into the pre-lesioned spinal cord in mice. Glia 36, 364–374.

Kitada, M., Rowitch, D.H., 2006. Transcription factor co-expression patterns indicate heterogeneity of oligodendroglial subpopulations in adult spinal cord. Glia 54, 35–46.

Lee, S.J., Lim, A.Y., Lim, I.J., Lim, T.C., Pho, R.W., 2008. Innervation of the face studied using modifications to Sihler's technique in a primate model. Plast. Reconstr. Surg. 121, 1188–1205.

McKay Hart, A., Brannstrom, T., Wiberg, M., Terenghi, G., 2002. Primary sensory neurons and satellite cells after peripheral axotomy in the adult rat: timecourse of cell death and elimination. Exp. Brain Res. 142, 308–318.

Mimura, T., Dezawa, M., Kanno, H., Sawada, H., Yamamoto, I., 2004. Peripheral nerve regeneration by transplantation of bone marrow stromal cell-derived Schwann cells in adult rats. J. Neurosurg. 101, 806–812.

Mligiliche, N.L., Tabata, Y., Kitada, M., Endoh, K., Okamato, K., Fujimoto, E., Ide, C., 2003. Poly lactic acid-caprolactone copolymer tube with a denatured skeletal muscle segment inside as a guide for peripheral nerve regeneration: a morphological and electrophysiological evaluation of the regenerated nerves. Anat. Sci. Int. 78, 156–161.

Nagane, K., Kitada, M., Wakao, S., Dezawa, M., Tabata, Y., 2009. Practical induction system for dopamine-producing cells from bone marrow stromal cells using spermine-pullulan-mediated reverse transfection method. Tissue Eng. Part A 15, 1655–1665.

Pittenger, M.F., Mackay, A.M., Beck, S.C., Jaiswal, R.K., Douglas, R., Mosca, J.D., Moorman, M.A., Simonetti, D.W., Craig, S., Marshak, D.R., 1999. Multilineage potential of adult human mesenchymal stem cells. Science 284, 143–147.

Plant, G.W., Chirila, T.V., Harvey, A.R., 1998. Implantation of collagen IV/poly(2-hydroxyethyl methacrylate) hydrogels containing Schwann cells into the lesioned rat optic tract. Cell Transplant. 7, 381–391.

Prockop, D.J., 1997. Marrow stromal cells as stem cells for nonhematopoietic tissues. Science 276, 71–74.

Radtke, C., Vogt, P.M., 2009. Peripheral nerve regeneration: a current perspective. Eplasty 9, e47.

Roth, T.M., Ramamurthy, P., Ebisu, F., Lisak, R.P., Bealmear, B.M., Barald, K.F., 2007. A mouse embryonic stem cell model of Schwann cell differentiation for studies of the role of neurofibromatosis type 1 in Schwann cell development and tumor formation. Glia 55, 1123–1133.

Shimizu, S., Kitada, M., Ishikawa, H., Itokazu, Y., Wakao, S., Dezawa, M., 2007. Peripheral nerve regeneration by the in vitro differentiated-human bone marrow stromal cells with Schwann cell property. Biochem. Biophys. Res. Commun. 359, 915–920.

Someya, Y., Koda, M., Dezawa, M., Kadota, T., Hashimoto, M., Kamada, T., Nishio, Y., Kadota, R., Mannoji, C., Miyashita, T., Okawa, A., Yoshinaga, K., Yamazaki, M., 2008. Reduction of cystic cavity, promotion of axonal regeneration and sparing, and functional recovery with transplanted bone marrow stromal cell-derived Schwann cells after contusion injury to the adult rat spinal cord. J. Neurosurg. Spine 9, 600–610.

Torigoe, K., Tanaka, H.F., Takahashi, A., Awaya, A., Hashimoto, K., 1996. Basic behavior of migratory Schwann cells in peripheral nerve regeneration. Exp. Neurol. 137, 301–308.

Vukovic, J., Plant, G.W., Ruitenberg, M.J., Harvey, A.R., 2007. Influence of adult Schwann cells and olfactory ensheathing glia on axontarget cell interactions in the CNS a comparative analysis using a retinotectal cograft model. Neuron Glia Biol. 3, 105–117.

Xu, Y., Liu, Z., Liu, L., Zhao, C., Xiong, F., Zhou, C., Li, Y., Shan, Y., Peng, F., Zhang, C., 2008. Neurospheres from rat adipose-derived stem cells could be induced into functional Schwann cell-like cells in vitro. BMC Neurosci. 9, 21.

Optimization of transmission scan duration for ^{15}O PET study with sequential dual tracer administration using N-index

Nobuyuki Kudomi · Hiroshi Watabe ·
Takuya Hayashi · Hisashi Oka · Yoshinori Miyake ·
Hidehiro Iida

Abstract

Purpose Cerebral blood flow (CBF), oxygen extraction fraction (OEF) and cerebral metabolic rate of O_2 (CMRO$_2$) can be quantified by PET with the administration of $H_2^{15}O$ and $^{15}O_2$. Recently, a shortening in the duration of these measurements was achieved by the sequential administration of dual tracers of $^{15}O_2$ and $H_2^{15}O$ with PET acquisition and integration method (DARG method). A transmission scan is generally required for correcting photon attenuation in advance of PET scan. Although the DARG method can shorten the total study duration to around 30 min, the transmission scan duration has not been optimized and has possibility to shorten its duration. Our aim of this study was to determine the optimal duration for the transmission scan. We introduced 'N-index', which estimates the noise level on an image obtained by subtracting two statistically independent and physiologically equivalent images. The relationship between noise on functional images and duration of the transmission scan was investigated by N-index.

Methods We performed phantom studies to test whether the N-index reflects the pixel noise in a PET image. We also estimated the noise level by the N-index on CBF, OEF and CMRO$_2$ images from DARG method in clinical patients, and investigated an optimal true count of the transmission scan.

Results We found tight correlation between pixel noise and N-index in the phantom study. By investigating relationship between the transmission scan duration and N-index value for the functional images by DARG method, we revealed that the transmission data with true counts of more than 40 Mcounts results in CBF, OEF, and CMRO$_2$ images of reasonable quantitative accuracy and quality.

Conclusion The present study suggests that further shortening of DARG measurement is possible by abridging the transmission scan. The N-index could be used to determine the optimal measurement condition when examining the quality of image.

Keywords Transmission scan · PET · O-15 gas · Image quality

N. Kudomi
Department of Medical Physics, Faculty of Medicine,
Kagawa University, Mikichou, Kitagun,
Kagawa 761-0793, Japan

H. Watabe (✉)
Department of Molecular Imaging in Medicine,
Osaka University Graduate School of Medicine, 2-2 Yamadaoka,
Suita, Osaka 565-0871, Japan
e-mail: watabe@mi.med.osaka-u.ac.jp

N. Kudomi · H. Watabe · T. Hayashi · H. Iida
Department of Investigative Radiology,
Advanced Medical-Engineering Center,
National Cardiovascular Center-Research Institute,
5-7-1, Fujishirodai, Suita, Osaka 565-8565, Japan

H. Oka · Y. Miyake
Department of Radiology, National Cardiovascular Center,
Hospital, 5-7-1, Fujishirodai, Suita, Osaka 565-8565, Japan

Introduction

Cerebral blood flow (CBF), oxygen extraction fraction (OEF) and cerebral metabolic rate of oxygen (CMRO$_2$) images have facilitated the understanding of the pathophysiological basis of cerebro-vascular disorders, and these images can be quantitatively measured using positron emission tomography (PET) with bolus administrations of ^{15}O-labeled oxygen ($^{15}O_2$) and water ($H_2^{15}O$) [1]. In the conventional three-step method [1–3], these functional

Springer

images were measured with separate scans for three tracers of $C^{15}O$ for cerebral blood volume (CBV), $H_2^{15}O$ for CBF and $^{15}O_2$ for CMRO$_2$, and there were additional waiting times between the scans in order to avoid the contamination of the previous tracer on the PET data. Therefore, the measurement process required a relatively long duration of around 1 h in the conventional method. Recently, the duration of the CBF, OEF and CMRO$_2$ measurements was shortened using a dual tracer autoradiography (DARG) method [4]. The DARG method is characterized by sequentially administrating dual tracers of $^{15}O_2$ and $H_2^{15}O$ typically for 3 min interval during a single PET scan. When compared with the conventional three-step method, the DARG method can shorten the total study period to approximately 30 min for the set of CBV, CBF, OEF and CMRO$_2$ measurements while maintaining the image quality and quantitative accuracy.

In order to shorten the examination period even more, one option is to eliminate the CO scan which is used to correct for radioactivity in vascular space [5]. The other is to shorten the duration of the transmission scan, which is required to correct the attenuation of the number of pairs of emitted 511 keV photons in the materials of brain or other, to quantitatively estimate the radio-tracer concentrations. Usually, transmission scan is performed with external ^{68}Ge sources [6, 7]. By prolonging the duration of transmission scan, the accuracy of attenuation correction (AC) will be improved, which results in better quality and accuracy of the functional images although a patient receives additional radiation exposures. In contrast, by shortening the duration of the transmission scan, the functional images might be deteriorated due to lack of statistics. Thus, optimization of transmission scan duration is needed. Because the ^{68}Ge rod sources radioactively decay with a half-life of 270.95 days, the optimal transmission scan duration depends on the radioactivity of the ^{68}Ge source and should be determined by the true transmission scan count. To determine the optimal true count of the transmission scan, quantitative accuracy (bias) and image quality (noise on image) of the CBF, OEF and CMRO$_2$ images must be considered. The quantitative accuracy can be evaluated by comparing two images generated from different transmission scan durations. Noise equivalent counts, NEC, is often used index to evaluate noise in PET image. However, by the NEC, noise propagation from the transmission scan cannot be assessed. Alternatively, to determine the quality of images, one can perform replicated PET measurements and evaluate pixel-wise standard deviation (SD) from these images [8]. Acquiring multiple images, however, are not practical, because measurement conditions such as the administration dose and physiological state cannot be equivalent across replicated measurements.

In this study, in order to evaluate image quality, we introduced an 'N-index' to define the noise level in an image. The validity of the N-index was tested using the Hoffman brain phantom [9]. In order to determine the optimal true count for the transmission scan, the introduced N-index was used to evaluate the noise level in the CBF, OEF and CMRO$_2$ images obtained from actual PET data with DARG method for patients with cerebro-vascular disease.

Materials and methods

Phantom studies for validation of N-index

It has been reported that the pixel-wise SD of a PET image reconstructed by the filtered backward projection (FBP) method was spatially uniform even in a nonhomogenous region [10]. On the basis of this suggestion, if we obtain two images of the same object with same activity concentration level from two independent scans or procedures, a spatial distribution of pixel values in the subtracted image between those two images has zero mean and its variation is related to the noise level of the images. The N-index is defined as the SD of the spatial distribution of the subtracted image.

To verify whether the N-index can be used as an index for noise level, the computed N-index was compared with the pixel-wise SD value of a PET image obtained from scanning a non-uniform object. We performed a PET experiment using the Hoffman brain phantom [9] filled with $^{18}F_2$ diluted in water. An ECAT EXACT HR (CTI Inc. Knoxville, USA) was used as the PET scanner, and the emission scan acquisition in the 2D mode was repeated every hour. Seven scans were performed. Before the first scan, approximately 207 MBq of $^{18}F_2$ with half-life of 109.8 min, water was injected. Each scan comprised 5 s × 50 frames and the total acquired time was 250 s so that the calculated image count at each location must be almost constant across frames ($\sim 0.05\%$ change between adjacent frames and $\sim 3\%$ between the first and last frames). 72 h after the first scan (when the radioactivity of ^{18}F became negligible), two 10-min transmission scans were performed.

Two AC maps were created to correct the attenuation using the data from the two 10-min transmission scans. Using these AC maps, two dynamic images were reconstructed by employing the FBP method from the same sinogram data. Corrections for randoms, dead time, scatters, and radioactivity decay to the start time of the first scan were applied, and the Gaussian filter with a filter width of 7 mm was used. For the obtained images, we defined the jth pixel value as $x_{i,j}^{n,k}$ with the kth frame ($k = 1, 2, \ldots, 50$) at nth scan

($n = 1, 2,...,7$) with ith AC map ($i = 1, 2$). Each image had a matrix size of $128 \times 128 \times 47$ with a pixel size of $1.8 \times 1.8 \times 3.38$ mm.

The pixel-wise SD images ($s_{i,j}^n$) were computed from all the 50 frames of the dynamic images as;

$$s_{i,j}^n = \text{SD}_{k=1,...,50}[x_{i,j}^{n,k}] \qquad (1)$$

where, $\text{SD}_{k \in K}[y_k]$ is defined as a standard deviation of y_k over K.

We calculated N-indices from two datasets to test equivalence of N-index to pixel-wise SD when amount of data change in terms of either scan duration or activity concentration as: (a) one frame data of duration 5 s and (b) 25 frames data of duration 125 s. For the dataset (a), a subtracted image ($I_j^{n,5s}$) was created by subtracting the 24th frame data with the first AC map from the 25th frame data with the second AC map as:

$$I_j^{n,5s} = x_{1,j}^{n,25} - x_{2,j}^{n,24}. \qquad (2)$$

The reason that we selected the 24th and 25th frames for the subtraction was to minimize the influence of physical decay in the pixel value. For the dataset (b), even-numbered frames with the first AC map and odd-numbered frames with the second AC map were summed in order to obtain two independent (but must be identical in terms of the radioactivity count at each location) images. By subtracting the two images, the subtracted image was created as:

$$I_j^{n,125s} = \frac{1}{25}\sum_{k \in \text{odd}} x_{1,j}^{n,k} - \frac{1}{25}\sum_{k \in \text{even}} x_{2,j}^{n,k}. \qquad (3)$$

The reason that we summed the frames alternately was to minimize the influence of physical decay in the pixel value. The subtracted image has a mean value that is approximately and uniformly zero.

A circular region of interest (ROI) (10.7 cm in diameter, 3620 pixels) was placed in the brain region on a slice at the level of thalamus. The mean SD value (M_{SD}^n) of $s_{i,j}^n$ and the N-index ($NI^{n,t}$) of $I^{n,t}$ inside the ROI were calculated and compared.

Subjects and PET procedure

For the CBF and $CMRO_2$ measurements, we performed a series of PET scans on six human subjects with cerebrovascular disease ($n = 6$, age = 69 ± 3 years, body weight = 64 ± 4 kg). The DARG approach [4, 11] was employed to compute the CBF and $CMRO_2$ images. An ECAT EXACT 47 (CTI Inc. Knoxville, USA), equipped with three rotating ^{68}Ge–^{68}Ga rod sources was used as the PET scanner. The PET procedures were approved by the ethics committee of the National Cardiovascular Center.

Transmission scans with multiple frames (60 s $\times$ 9 frames and 30 s $\times$ 2 frames) were performed for 10 min. After the transmission scan, a 4-min static emission scan along with $C^{15}O$ administration was performed. Subsequently, a dynamic DARG $H_2^{15}O$–$^{15}O_2$ scan [4] was started with the sequential administration of gaseous $^{15}O_2$ (3000 MBq, 1-min inhalation) followed by $H_2^{15}O$ (1110 MBq, intra-venous injection into the right brachial vein) administration after 6 min. The DARG scan sequence comprised 10 s $\times$ 6 frames, 20 s $\times$ 6 frames, 30 s $\times$ 4 frames, 10 s $\times$ 4 frames, 5 s $\times$ 10 frames and 15 s $\times$ 2 frames. All data were acquired in the 2D mode with extended septa.

To obtain the arterial input function, a catheter was inserted into the brachial artery, and blood was withdrawn at a flow rate of 4 ml/min during each emission PET scan. The arterial blood time activity curve (TAC) was continuously monitored using a GSO input function monitor [12].

Data processing

From the multi-frame transmission data with 11 frames, two sets for 30, 60, 120, 180, 240 and 300 s were generated by adding the frames and avoiding duplications. In addition, the sum of the transmission data with a duration of 600 s was obtained. On the basis of the obtained transmission data and the blank scan data, 13 AC maps were generated defined as AC_i^t, where $i = 1, 2$ (index of the sets), and $t = 30, 60, 120, 180, 240, 300$ s (transmission data time duration) and AC_1^{600s}.

Along with detector normalization, the static images for the $C^{15}O$ scan and the dynamic image for the $^{15}O_2$–$H_2^{15}O$ emission scan sinograms were corrected for dead time and radioactive decay in each frame. Tomographic images were reconstructed using these corrected sinograms obtained by the FBP method with 7-mm Gaussian filtering. AC was applied to the $C^{15}O$ static image using the AC map obtained from the 600-s transmission data, (i.e., AC_1^{600s}), and to the $^{15}O_2$–$H_2^{15}O$ dynamic image using all the generated AC map data of AC_i^t. Thus, 13 dynamic images were obtained. The pixel value was defined as $x_{j,(i,t)}^k$ for jth pixel value with kth frame using AC_i^t. A scatter correction was also applied. The reconstructed dynamic images had a matrix size $128 \times 128 \times 47$ with a pixel size of $1.8 \times 1.8 \times 3.38$ mm.

The following three steps were employed to sum up a part of the reconstructed dynamic image for the $^{15}O_2$–$H_2^{15}O$ scan during each oxygen (180 s from the start of oxygen inhalation, indicated as: $k \in O_2$) and water (120 s from the increase in the brain tissue TAC, indicated as: $k \in H_2O$) phase. First, all the frames were summed as: $\sum^{k \in O_2,\text{all}} x_{j,(1,t)}^k$ and $\sum^{k \in H_2O,\text{all}} x_{j,(1,t)}^k$. Second, all the even-numbered frames

were summed as: $\sum^{k\in O_2,\text{even}} x^k_{j,(2,t)}$ and $\sum^{k\in H_2O,\text{even}} x^k_{j,(2,t)}$. Lastly, all the odd-numbered frames were summed as: $\sum^{k\in O_2,\text{odd}} x^k_{j,(1,t)}$ and $\sum^{k\in H_2O,\text{odd}} x^k_{j,(1,t)}$. We assumed two images summed with even- and odd-numbered frames are physiologically and quantitatively equivalent and statistically independent.

Arterial blood TACs were corrected for radioactivity decay and dispersion ($\tau = 4$ s) [4, 13, 14] and delay [3, 4, 15] further, the $^{15}O_2$ and $H_2^{15}O$ contents were separated [11]. The obtained $^{15}O_2$ and $H_2^{15}O$ arterial TACs were used as the water and oxygen input functions as $A_W(t)$ and $A_O(t)$, respectively.

Sets of CBF, OEF and CMRO$_2$ images were generated using the DARG approach as described previously [4] by using a set of summed images in both the oxygen and water phases ($\sum^{k\in O_2,\rho} x^k_{j,(1,t)}$ and $\sum^{k\in H_2O,\rho} x^k_{j,(1,t)}$, where ρ indicates the rule of sum, i.e., all, even or odd), $^{15}O_2$ and $H_2^{15}O$ input functions [$A_W(t)$ and $A_O(t)$] and cerebral blood volume (CBV) image that was obtained from the C^{15}O scan data [3, 4]. This procedure was repeated for all sets of images and the functional images for jth pixel were obtained as: $CBF^\rho_{j,(i,t)}$, $OEF^\rho_{j,(i,t)}$ and $CMRO2^\rho_{j,(i,t)}$, where indices (i, t) are same as those for AC, and ρ is the rule of sum.

Dependency of quantitative CBF/OEF/CMRO$_2$ accuracy on the transmission true counts

An ROI was placed on the frontal, temporal and parietal cortical region (5000–10000 pixels) of the image and the CBF, OEF and CMRO$_2$ values were extracted from all the datasets. The mean of these extracted values was expressed as the percent difference between the values obtained from the functional images computed with AC^t_1 and with AC^{600s}_1 for all datasets obtained from the emission data as:

$$\frac{R\left[\text{Func}^{\text{all}}j_{,(1,t)}\right] - R\left[\text{Func}^{\text{all}}_{j,(1,600s)}\right]}{R\left[\text{Func}^{\text{all}}_{j,(1,600s)}\right]} \times 100\% \quad (4)$$

where R indicates mean pixel value inside the ROI and Func indicates either CBF, OEF or CMRO$_2$.

Dependency of CBF/OEF/CMRO$_2$ image quality on the transmission true counts

Subtracted images were created by subtracting the functional images between even- and odd-numbered frames as;

$$I^{\text{Func}}_{j,t} = \text{Func}^{\text{even}}_{j,(1,t)} - \text{Func}^{\text{odd}}_{j,(2,t)} \quad (5)$$

for the jth pixel. The N-index in the ROI, placed on the frontal, temporal and parietal cortical region as above, for these subtracted images were calculated as:

$$\text{NI}^t_{\text{Func}} = \text{SD}_{j\in\text{ROI}}\left[I^{\text{Func}}_{j,t}\right]. \quad (6)$$

The obtained N-indices were expressed as a function of the total true count of the transmission scan data.

Results

Phantom studies for validation of N-index

Figure 1 shows representative slices of the obtained images of mean, SD, and subtraction. The later scan has more noise due to count statistics, which can be observed in SD image and the subtracted images in Fig. 1. Despite the difference in the activity distribution, the SD image was almost uniform. The relationship between the mean value of the SD image (M_{SD}) and N-index (NI) in the same ROI

Fig. 1 Representative slices of the reconstructed images obtained from the phantom studies. The *first row* is averaged image, the *second row* is SD image, the *third row* is the subtracted image for the dataset (a), and the *fourth row* is the subtracted image for the dataset (b). *Each column* corresponds the images from nth scan (total seven scans)
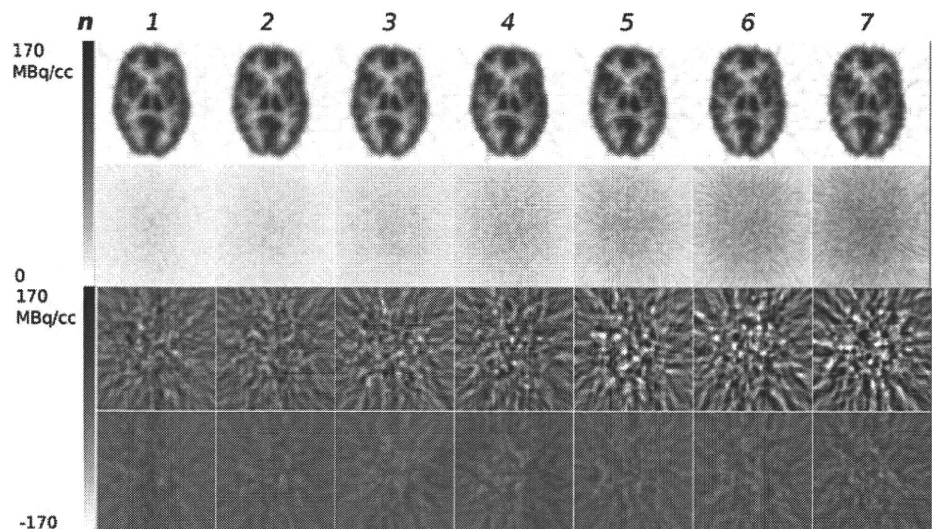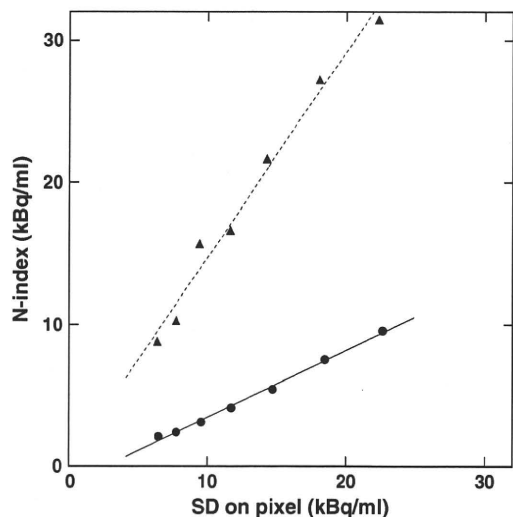
Fig. 2 The relationship between the mean SD value and *N*-index obtained from the subtracted image with the same ROI region of the brain phantom. The regression line was expressed as $y = 1.44x - 0.331$ (kBq/ml) ($r = 0.99$, $n = 7$). and $y = 0.47x - 1.29$ (kBq/ml) ($r = 0.99$, $n = 7$), for 5 s (*closed triangle*) and 125 s (*closed circle*) in calculating *N*-index, respectively

is shown in Fig. 2. The regression line is expressed as $NI = 1.44M_{SD} - 0.331$ (kBq/ml) ($r = 0.99$) and $NI = 0.47M_{SD} - 1.285$ (kBq/ml) ($r = 0.99$), where r is correlation coefficient, for the subtracted images obtained from the 5- and 125-s data, respectively. The results shown in Figs. 1 and 2 support the assumption that the SD of the pixel value is uniform in a non-homogeneous image that was reconstructed using the FBP method. Furthermore, the present *N*-index was correlated with the SD and could be employed to compare the image qualities.

Dependency of quantitative CBF/OEF/CMRO$_2$ accuracy on the transmission true counts

Figure 3 shows the percent difference in the CBF (a), OEF (b) and CMRO$_2$ (c) values when compared with those computed using the 10-min AC map. The results show that the quantitative values obtained during the CBF, OEF and CMRO$_2$ measurements are almost identical, namely, difference was <5% to those obtained when AC was performed using the transmission data containing true counts more than 40 Mcounts.

Dependency of the CBF/OEF/CMRO$_2$ image quality on the transmission true counts

Figure 4 shows the *N*-indices in the CBF (a), OEF (b) and CMRO$_2$ (c) images, as a function of the number of true counts of the transmission data. The present results show that the qualities of the CBF, OEF and CMRO$_2$ images
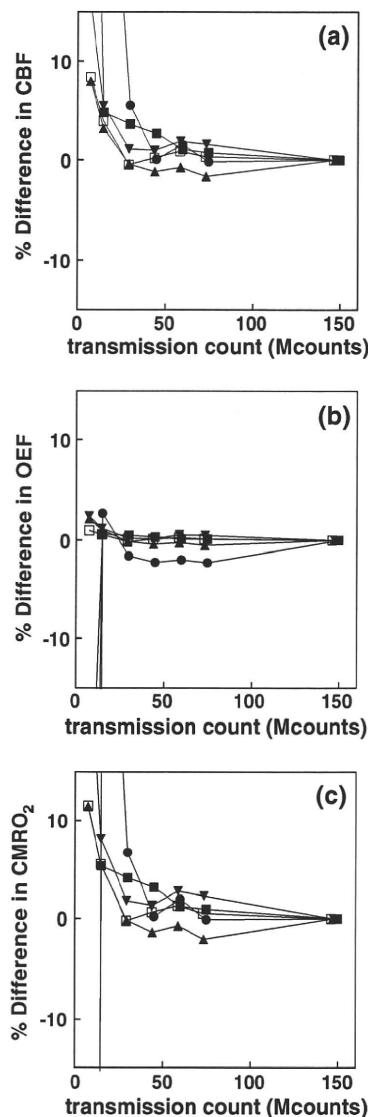

Fig. 3 Percent difference in the CBF, OEF and CMRO$_2$ values when compared with those obtained from the 10-min transmission data, as a function of the true counts of the transmission data. Each type of *symbol* corresponds to each subject ($n = 6$). The indicated values were extracted from the ROI in the frontal, parietal and temporal cortex regions

were almost equal to those in which the true counts of the transmission data used exceeded 40 Mcounts.

Discussion and conclusion

Our purpose of this study was to shorten the transmission scan duration for ^{15}OPET study with DARG measurement. By evaluating bias and noise on the functional images of the CBF, OEF and CMRO$_2$ due to noise in transmission data, optimal transmission true count in DARG measurement was
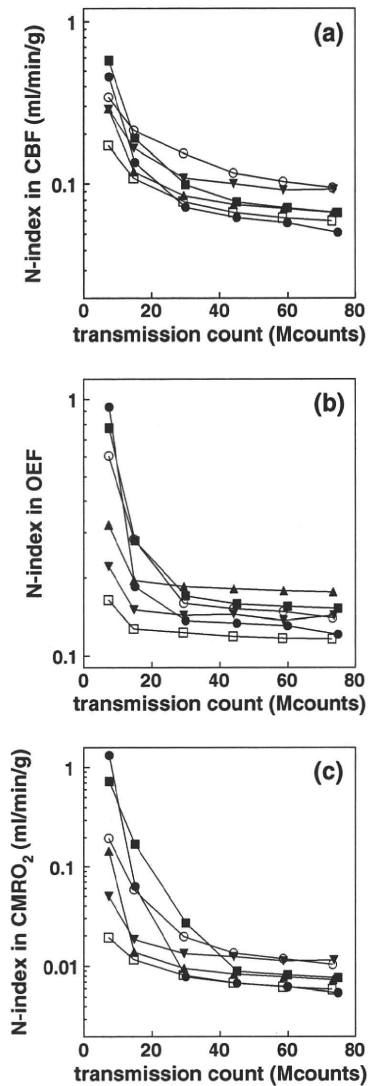
Fig. 4 The *N*-indices for the CBF, OEF and CMRO₂ images that were obtained from various true counts of the transmission data as a function of the true counts of the transmission data. Each type of *symbol* corresponds to each subject (*n* = 6). The *symbols* used and ROI are the same as that used for Fig. 3

determined. We found 40 Mcounts of the true count in the transmission scan was optimal, and consequently, we were able to shorten the total duration of the DARG examination.

We introduced the *N*-index to compare the noise level on inhomogeneous functional images. The benefit of using *N*-index is that by one index number, one can characterize the noise in functional image derived from PET data and DARG measurement which have complex noise propagations from several error sources. The validity of the *N*-index was tested in the phantom study. We found tight correlation between pixel noise and the *N*-index.

The present result using the brain phantom supported the assumption that the SD of a pixel value was spatially

uniform even in a non-homogeneous region of an FBP reconstructed image (Fig. 1). Furthermore, the regression line between the SD value from the statistically obtained SD image and the *N*-index from the subtracted image for 5- and 125-s data were highly correlated (*r* = 0.99) (Fig. 2). The slope for 5-s data was approximately $\sqrt{2}$, where the SD of the image obtained by subtraction of two 5-s data (statistically corresponding to 10 s) could be expected to be $\sqrt{2}$ greater than that of the original image. For 125-s data, 1/5 of statistical noise compared to 5-s data is expected. However, *N*-index for 125-s data overestimated in 18% in average than expected. One possible reason of this overestimation is influence of inhomogeneity of the reconstructed image. Therefore, the *N*-index cannot be used to estimate absolute noise level in the image, but the *N*-index is still valid for study which compares relative noise levels among multiple images.

Using the *N*-index, we examined the change of image quality in the CBF, OEF and CMRO₂ as the noise level based on the change in the true counts of the transmission data. One of the advantages using the *N*-index is that it allows us to compare the noise level of non-uniform images such as that of the brain, using the data obtained by ordinal PET scan procedure. In order to investigate the noise level of the PET images using parameters other than the *N*-index, the PET scans must be replicated for a human subject. However, this appears unlikely due to the excessive radiation dose that would need to be administered to the subject. Furthermore, it might be quite hard to maintain the equivalent measurement conditions such as the radiation dose, as well as the physiological conditions of the subjects.

In this study, two implicit conditions were assumed: the SD on pixel value is uniform for the targeted region and odd-and even-numbered frames have the same statistical properties. The condition of uniform distribution of the SD on the functional image might not be microscopically fulfilled due to nature of nonlinearity of DARG method. However, in global, noise on the reconstructed image could be linearly propagated to the functional image and we considered this assumption was valid for computing the *N*-index. The *N*-index can be applied to other cases such as a variety of tracers and organs in order to examine the image quality as far as those conditions are satisfied. It should be noted that the CBF and CMRO₂ parametric images are required to be assessed quantitatively [16], thus the present study was validated with images reconstructed by FBP method. Limitation of the present method is that the *N*-index may not be applied to images such as those reconstructed by the maximum likelihood expectation maximization based algorithm, because the uniformity of SD across pixels is not guaranteed. However, a similar procedure of the present method still has possibility to be

applied, if, for example, coefficient of variation is uniform across pixels.

When N-index was estimated from two images with either emission or transmission data being common, the variation on image can be calculated as a sum of each variation and subtraction of covariance, canceling effect of noise from common data. Consequently, the N-index only reflects noise on either transmission or emission data. Thus, we estimated N-index by subtracting fully independent images. The validity of N-index could be tested in the phantom study using common transmission data; however, we still computed N-index using fully independent images, because the test should be done in the same conditions as the experimental study.

The present results showed that poor count statistics in transmission scanning resulted in significant bias in quantitative values of CBF, OEF and CMRO$_2$. As has been mathematically described [17], AC factor, i.e. blank/transmission is biased by factor of $(1 + 1/m)$, where m is a transmission count on a corresponding pixel. Therefore, the poorer the transmission scan count is, the higher the AC factor becomes. In view of image quality, noise in transmission data influences functional image as shown in Fig. 4. On the other hand, as indicated in Fig. 4, extra longer transmission scan gains no statistical benefit. The optimized transmission scan duration will be determined by relative noise level of the transmission data against the emission data.

In this paper, we used fixed duration of 600 s of the transmission scan for CO image, assuming little effect of noise on CO image. One reason for this assumption is that 50% error in CBV value derives around only 3% error in OEF and CMRO$_2$ images [4], suggesting 50% noise on CBV image resulting only 3% noise on OEF and CMRO$_2$ images. As shown in Fig. 4, the degree of noise on the OEF and CMRO$_2$ images are around 20–25%, and the level of noise is quite high compared to level of noise from CBV image.

Motion of subject, during a scan, could be a problem to calculate N-index. However, movement of a subject during a scan affects both the odd-and even-numbered frames simultaneously, and thus the statistical properties between two summed images will stay the same. Thus, motion of a subject during a scan might not be that critical with regards to the N-index, as far as the motion does not deteriorate the image used to assess the function of the targeted organ.

The comparison of the N-indices between subjects or between different functional images cannot be performed because the N-indices offer information of relative noise level but not absolute noise. Thus, a meaningful comparison can be made between images of the same subject and of the same cerebral function (such as CBF and CMRO$_2$).

It is generally accepted that accurate ACs require transmission scanning using external sources [6, 7], although there are excellent techniques designed to shorten or eliminate the transmission scan duration, such as the transmission-data-based segmented method for the AC map [18, 19] or the emission-based AC map calculation [20]. The present approach might be applicable to investigate the noise level in segmented or emission-based methods, which should enable us to further shorten the duration of a PET examination.

Boellaard et al. demonstrated the relationship between the transmission scan counts and phantom diameter, and they found that this relationship did not restrict the application of the count-based transmission scans for correcting the reduction in the rod source strength [21]. However, they indicated that when the subject is extremely small, a transmission scan based on an acquired number of true counts should not be applied. This is because the counts for lines of response not passing through the subject would increase. Further studies are required to determine the optimal examination conditions for such situations.

We found that the true counts of the transmission data exceeding 40 millions (corresponds to 3 min scan in this study) were appropriate for the CBF, OEF and CMRO$_2$ measurement by DARG method in terms of both quantitative accuracy and image quality, consequently we can shorten the examination duration for obtaining those images. Conventional DARG measurement in clinical study uses 10 min of transmission scan, while 9 min of emission scan of dual tracers of $^{15}O_2$ and $H_2^{15}O$, in addition to 4 min of $C^{15}O$ scan [22]. If one can shorten the transmission scan to 3 min, total scan duration is 16 min (30% reduction). Currently, another $C^{15}O$ scan for CBV correction with regards to the assessment of CBF, OEF and CMRO$_2$ is still required, an additional mathematical formulation strategy, like the basis function method [23] could eliminate this requirement [5].

In conclusion, we determined the required transmission true count that maintains the quantitative accuracy and image quality for PET studies with $H_2^{15}O$ and $^{15}O_2$. According to our results, the total study duration could be minimized by shortening the transmission scan. Although the obtained results in the present study were measurement condition specific, the N-index could be used to determine PET scanning procedures.

References

1. Mintun M, Raichle M, Martin W, Herscovitch P. Brain oxygen utilization measured with O-15 radiotracers and positron emission tomography. J Nucl Med. 1984;25:177–87.

2. Hatazawa J, Fujita H, Kanno I, Satoh T, Iida H, Miura S, et al. Regional cerebral blood flow, blood volume, oxygen extraction fraction, and oxygen utilization rate in normal volunteers measured by the autoradiographic technique and the single breath inhalation method. Ann Nucl Med. 1995;9:15–21.

3. Shidahara M, Watabe H, Kim K, Oka H, Sago M, Hayashi T, et al. Evaluation of a commercial PET tomograph-based system for the quantitative assessment of rCBF, rOEF and rCMRO2 by using sequential administration of 15O-labeled compounds. Ann Nucl Med. 2002;16:317–27.

4. Kudomi N, Hayashi T, Teramoto N, Watabe H, Kawachi N, Ohta Y, et al. Rapid quantitative measurement of CMRO(2) and CBF by dual administration of (15)O-labeled oxygen and water during a single PET scan—a validation study and error analysis in anesthetized monkeys. J Cereb Blood Flow Metab. 2005;25: 1209–24.

5. Kudomi N, Hayashi T, Watabe H, Iida H. Rapid CBF/CMRO$_2$ measurement in a single PET scan with dual tracer administration. J Cereb Blood Flow Metab. 2005;25:S672.

6. Bailey D. Transmission scanning in emission tomography. Eur J Nucl Med. 1998;25:774–87.

7. Ostertag H, Kbler W, Doll J, Lorenz W. Measured attenuation correction methods. Eur J Nucl Med. 1989;15:722–6.

8. Watabe H, Matsumoto K, Senda M, Iida HP. Performance of list mode data acquisition with ECAT EXACT HR and ECAT EXACT HR + positron emission scanners. Ann Nucl Med. 2006;20:189–94.

9. Hoffman E, Cutler P, Digby W, Mazziotta J. 3-D phantom to simulate cerebral blood flow and metabolic images for PET. IEEE Trans Nucl Sci. 1990;37:616–20.

10. Pajevic S, Daube-Witherspoon M, Bacharach S, Carson R. Noise characteristics of 3-D and 2-D PET images. IEEE Trans Med Imaging. 1998;17:9–23.

11. Kudomi N, Watabe H, Hayashi T, Iida H. Separation of input function for rapid measurement of quantitative CMRO$_2$ and CBF in a single PET scan with a dual tracer administration method. Phys Med Biol. 2007;52:1893–908.

12. Kudomi N, Choi E, Yamamoto S, Watabe H, Kim K, Shidahara M, et al. Development of a GSO detector assembly for a continuous blood sampling system. IEEE Trans Nucl Sci. 2003;50: 70–3.

13. Iida H, Kanno I, Miura S, Murakami M, Takahashi K, Uemura K. Error analysis of a quantitative cerebral blood flow measurement using H2(15)O autoradiography and positron emission tomography, with respect to the dispersion of the input function. J Cereb Blood Flow Metab. 1986;6:536–45.

14. Lammertsma A, Cunningham V, Deiber M, Heather J, Bloomfield P, Nutt J, et al. Combination of dynamic and integral methods for generating reproducible functional CBF images. J Cereb Blood Flow Metab. 1990;10:675–86.

15. Iida H, Higano S, Tomura N, Shishido F, Kanno I, Miura S, et al. Evaluation of regional differences of tracer appearance time in cerebral tissues using [15O] water and dynamic positron emission tomography. J Cereb Blood Flow Metab. 1988;8:285–8.

16. Ibaraki M, Miura S, Shimosegawa E, Sugawara S, Mizuta T, Ishikawa A, et al. Quantification of cerebral blood flow and oxygen metabolism with 3-dimensional PET and 15O: validation by comparison with 2-dimensional PET. J Nucl Med. 2007;49:50–9.

17. Freedman N, Bacharach S, Carson R, Price J, Dilsizian V. Effect of smoothing during transmission processing on quantitative cardiac PET scans. J Nucl Med. 1996;37:690–4.

18. Xu M, Luk W, Cutler P, Digby W. Local threshold for segmented attenuation correction of PET imaging of the thorax. IEEE Trans Nucl Sci. 1994;41:1532–7.

19. Xu M, Cutler P, Luk W. Adaptive, segmented attenuation correction for whole-body PET imaging. IEEE Trans Nucl Sci. 1996;43:331–6.

20. Weinzapfel B, Hutchins G. Automated PET attenuation correction model for functional brain imaging. J Nucl Med. 2001;42:483–91.

21. Boellaard R, Lingen Av, Balen Sv, Lammertsma A. Optimization of attenuation correction for positron emission tomography studies of thorax and pelvis using count-based transmission scans. Phys Med Biol. 2004;49:N31–8.

22. Iwanishi K, Watabe H, Hayashi T, Miyake Y, Minato K, Iida H. Influence of residual oxygen-15-labeled carbon monoxide radioactivity on cerebral blood flow and oxygen extraction fraction in a dual-tracer autoradiographic method. Ann Nucl Med. 2009;23:363–71.

23. Gunn R, Lammertsma A, Hume S, Cunningham V. Parametric imaging of ligand receptor binding in PET using a simplified reference region model. Neuroimage. 1997;6:279–87.

Multicenter Evaluation of a Standardized Protocol for Rest and Acetazolamide Cerebral Blood Flow Assessment Using a Quantitative SPECT Reconstruction Program and Split-Dose ^{123}I-Iodoamphetamine

Hidehiro Iida[1,2], Jyoji Nakagawara[1,3], Kohei Hayashida[1,4], Kazuhito Fukushima[1,5], Hiroshi Watabe[1,2], Kazuhiro Koshino[1,2], Tsutomu Zeniya[1,2], and Stefan Eberl[1,6]

[1]Dual-Table Autoradiography SPECT Research Group in Japan, Osaka, Japan; [2]National Cerebral and Cardiovascular Center–Research Institute, Osaka, Japan; [3]Nakamura Memorial Hospital, Sapporo, Japan; [4]Takeda Hospital, Kyoto, Japan; [5]National Cerebral and Cardiovascular Center–Hospital, Osaka, Japan; and [6]Royal Prince Alfred Hospital, Sydney, Australia

SPECT can provide valuable diagnostic and treatment response information in large-scale multicenter clinical trials. However, SPECT has been limited in providing consistent quantitative functional parametric values across the centers, largely because of a lack of standardized procedures to correct for attenuation and scatter. Recently, a novel software package has been developed to reconstruct quantitative SPECT images and assess cerebral blood flow (CBF) at rest and after acetazolamide challenge from a single SPECT session. This study was aimed at validating this technique at different institutions with a variety of SPECT devices and imaging protocols. **Methods:** Twelve participating institutions obtained a series of SPECT scans on physical phantoms and clinical patients. The phantom experiments included the assessment of septal penetration for each collimator used and of the accuracy of the reconstructed images. Clinical studies were divided into 3 protocols, including intrainstitutional reproducibility, a comparison with PET, and rest–rest study consistency. The results from 46 successful studies were analyzed. **Results:** Activity concentration estimation (Bq/mL) in the reconstructed SPECT images of a uniform cylindric phantom showed an interinstitution variation of $\pm5.1\%$, with a systematic underestimation of concentration by 12.5%. CBF values were reproducible both at rest and after acetazolamide on the basis of repeated studies in the same patient (mean $\pm$ SD difference, -0.4 ± 5.2 mL/min/100 g, $n = 44$). CBF values were also consistent with those determined using PET (-6.1 ± 5.1 mL/min/100 g, $n = 6$). **Conclusion:** This study demonstrates that SPECT can quantitatively provide physiologic functional images of rest and acetazolamide challenge CBF, using a quantitative reconstruction software package.

Key Words: ^{123}I-iodoamphetamine; cerebral blood flow; acetazolamide; SPECT; vascular reactivity; quantitation

J Nucl Med 2010; 51:1624–1631
DOI: 10.2967/jnumed.110.078352

Current clinical practice using SPECT relies largely on interpretation of qualitative images reflecting physiologic function. Quantitative functional parametric images may be obtained by applying mathematic modeling to SPECT data corrected for attenuation and scatter. Quantitative regional cerebral blood flow (CBF) (1–3) and cerebral vascular reactivity (CVR) in response to acetazolamide challenge (4–6) have been obtained with these techniques. One major application of such quantitative SPECT (QSPECT) approaches is the evaluation of ischemic status in patients with occlusion or stenosis in their middle cerebral arteries, to provide prognostic information of the outcome of revascularization therapies (7). Quantitative analysis in SPECT has also been demonstrated in the assessment of binding potential for several neuroreceptor ligands (8,9), for the quantitative assessment of regional myocardial perfusion (10,11), and for the assessment of radioaerosol deposition and clearance in healthy and diseased lungs (12). However, providing the standardized quantitative approach required for multicenter clinical trials has so far received only limited attention. Challenges remain in providing consistent quantitative data across institutions using a variety of SPECT equipment and vendor-specific reconstruction strategies (13). This limitation is attributed to a lack of standardized procedures in the reconstruction software offered by vendors, particularly in terms of correcting attenuation and scatter. Kinetic modeling for physiologic parameter estimation is also not part of the vendors' standard SPECT software. Although separate packages can be purchased for this purpose, they are not integrated and are flexible general-purpose packages, requiring considerable skill and knowledge to effectively use. Thus, they are not ideal for routine clinical use.

Scatter and attenuation occur in the object and are thus object-dependent but are not dependent on the geometry of the imaging equipment (14). Therefore, once a software program is developed to provide accurate image reconstruction with compensation for both attenuation and scatter, the

program should be able to provide quantitative images that are intrinsically independent of the geometric design of SPECT cameras. This is an attractive feature of SPECT for multicenter clinical studies.

From the various techniques available to correct for attenuation (15) and scatter (16), one feasible approach for clinical studies is based on a combination of attenuation correction, incorporated into the ordered-subset expectation maximization (OSEM) reconstruction (17), and scatter correction by the transmission-dependent convolution subtraction (TDCS) originally proposed by Meikle et al. (18). This approach has been extensively investigated by our group (11,19) for ^{99m}Tc for studies of the brain and heart (18,20) and also in cardiac ^{201}Tl studies (11,21). A recent study also demonstrated the accuracy of this approach in a combined SPECT/CT system (22). By incorporating a correction for collimator septal penetration by high-energy emissions, one can also make the technique applicable to ^{123}I (19).

The QSPECT reconstruction approach has estimated CBF images at rest in a clinical setting (11) and quantified CVR by measuring CBF at rest and after vasodilation in a single SPECT session. This was accomplished by using the dual-table autoradiographic (DTARG) method and a dual administration of ^{123}I-iodoamphetamine (23). In those studies, corrections for attenuation and scatter appeared to be essential for generating quantitative CBF maps that were consistent with those generated by ^{15}O-water PET (11,23).

These studies were, however, validated in a single institution using a limited range of SPECT systems, and the general applicability of this technique for different SPECT systems had yet to be fully established. Thus, the aim of this study was to verify that analysis of data with a standardized reconstruction package incorporating attenuation and scatter correction can provide reproducible results across multiple institutions for quantitative rest and acetazolamide challenge CBF estimation from a single SPECT session.

MATERIALS AND METHODS

Institutions and Subjects

The 12 participating institutions were clinical centers and generally did not have scientific staff dedicated to nuclear medicine software or hardware development. Standard, vendor-supplied software was used for the collection of the studies, with unmodified scanners and collimators clinically used for brain studies. The acquired data were reconstructed with the program package developed for this project. Manufacturers and models of camera systems and the number of detectors and collimators (including fanbeam or parallel hole) used by the institution are listed in Supplemental Table 1 (supplemental materials are available online only at http://jnm.snmjournals.org). All institutions performed experiments on physical phantoms according to the protocol described in the "Phantom Experiment" section. Of the 12 institutions, 9 obtained patient scans, whereas the remaining 3 provided only phantom data. Clinical studies were approved by institutions' ethics committees or followed guidelines for clinical research protocols authorized by the institution. All subjects at each institution gave written informed consent.

The clinical studies were divided into 3 protocols: intrainstitutional, intrasubject reproducibility (reproducibility); comparison with PET (vs. PET); and intrascan consistency of the dual-time-point split-dose (rest–rest). Studies were excluded from the analysis if there was severe patient motion during one of the studies or if there were changes in the condition of the patients between the first and second studies likely to lead to changes in CBF.

Eight institutions (institutions 1, 3, 4, 6, 8, 9, 11, and 12) participated in the reproducibility arm, in which quantitative CBF values measured on separate days were compared. In this arm, all patients experienced unilateral or bilateral stenosis or occlusion in the extracranial internal carotid artery. The patients' ages ranged from 43 to 81 y (mean ± SD, 65 ± 9 y). A total of 31 studies in this protocol were analyzed. Four patients had to be excluded from the analysis—2 because of significant changes in their pathophysiologic status between the studies and 2 because of severe motion and mispositioning in the scanner.

One institution (institution 4) performed the versus-PET studies. CBF values obtained by the DTARG method were compared with those by ^{15}O-water and PET. Studies were performed on 6 patients (5 men, 1 woman; age range, 71–74 y; mean age ± SD, 72 ± 1 y) with stenosis or occlusion of the extracranial internal carotid artery unilaterally ($n = 3$) or bilaterally ($n = 3$).

Two institutions (institutions 2 and 12) provided data for the rest–rest comparison. Five patients from institution 2 had chronic cerebral infarction, whereas 4 subjects from institution 12 had no sign of cerebral disease. Patients' ages ranged from 32 to 72 y (mean ± SD, 52 ± 15 y); 5 patients were men and 4 women.

Phantom Experiment

Three experiments were performed by each institution using the SPECT camera fitted with the collimators normally used in clinical brain studies. The first scan determined the absolute sensitivity or the becquerel calibration factor (BCF) of the reconstructed images. For 10 min, a 360° projection set was acquired of a syringe filled with a ^{123}I-iodoamphetamine solution of known radioactivity and placed at the center of the field of view. The syringe was supplied by Nihon-Medi Physics, and its radioactivity was calibrated to 111 MBq at noon on the day before the experiment, with an accuracy better than 3%, decaying to approximately 30 MBq at the time of the experiment, avoiding the dead time of the camera. The BCF was determined by dividing the absolute radioactivity by the total counts for the syringe region in the reconstructed image.

The second experiment determined the collimator septal penetration contribution (24) from high-energy photons into the primary 159-keV energy window for ^{123}I. A line-spread function was obtained from the projection data of a line source filled with ^{123}I-iodoamphetamine. The septal penetration was determined from the background level as described previously (19). A projection line-spread function was also generated from this line source placed in a water-filled cylindric phantom (diameter, 16 cm).

The third experiment used a 16-cm-diameter, 15-cm-long uniform cylindric phantom. The whole radioactivity used for the BCF determination was diluted into the phantom, and projection data were acquired for 30 min, using the clinical scan protocols described in the "Clinical Studies" section. The radioactivity concentration (counting rate per unit mass) of an approximately 0.3-mL sample from the phantom was measured using the well counters available at the various institutions. Both NaI- and plastic scintillator–based well counters were used (Supplemental Table